Improving the Circularization Efficiency, Stability and Translatability of Circular RNA by circDesign

Congcong Xu[1,†], Liang Zhang[2,†], Weiyun Wang[1,†], Yuying Tang[1], Qiuhe Wang[1], Jinqi An[1], Heng Xu[1], Yun Ge[1], Hanfei Zhu[1], He Wang[1], Bin Li[1], Xiaotian Wang[1], Xuhui Qiu[1], Mingyun Shen[1], Geng Chen[1], Haifa Shen[1, $], Liang Huang[3, $], Hangwen Li[1,4, $]

[1]StemiRNA Therapeutics, Shanghai, China
[2]China Pharmaceutical University, Nanjing, China
[3]Coderna.ai, Sunnyvale, CA, USA
[4]Shanghai East Hospital, Shanghai, China

[$]Correspondence to:

Liang Huang (liang.huang.sh@gmail.com)
Haifa Shen (shf@stemirna.com)
Lead contact: Hangwen Li (lihangwen@stemirna.com)

†These authors contributed equally.

Abstract

Synthetic circular RNA (circRNA) has recently emerged as the next generation RNA technology for vaccine and drug development, featuring its uniqueness in a closed-loop structure and cap-independent translation mechanism. However, rational design and optimization of circRNA to improve its stability and protein coding potential remains challenging due to lack of structure prediction tool and sequence design algorithm for endless circular-shaped RNA. In this study, we presented circDesign, a computational approach to achieve optimal design of the circRNA with enhanced circularization efficiency, stability, and translatability. Using rabies virus glycoprotein (RABV-G) and varicella-zoster virus (VZV) glycoprotein gE as the exemplified antigens, we demonstrated that optimized circRNAs encoding corresponding antigens exhibited higher stability and protein translation efficiency *in vitro*. Formulated by proprietary delivery system lipopolyplex (LPP), the optimized circRNA vaccines encoding RABV-G or VZV gE antigen further elicited enhanced humoral and cellular *in vivo* immune responses in mice. Taken together, this circular RNA design approach provided a general strategy to leverage the capability of circRNA as next generation vaccines or therapeutics.

Keywords: circular RNA; circDesign; Algorithm; RNA vaccine; Rabies vaccine; Varicella-zoster virus vaccine; Lipopolyplex

Introduction

Rational sequence design of messenger RNAs (mRNAs) is of pivotal importance to maximize the potency of mRNA vaccines or therapeutics[1]. Optimization of conventional linear mRNA usually involves 5'- & 3'-untranslated region (UTR) and open reading frame (ORF), which could be simply achieved by combining naturally occurring UTR pair with codon optimized ORF region[2, 3]. As exemplified by Moderna's mRNA-1273 and BioNTech's BNT162b2 COVID-19 mRNA vaccines, the optimized ORF was directly flanked with previously screened UTR pair[4]. Besides, it was reported the functional half-life of mRNA dictates its *in vivo* performance as the translation efficiency and stability of mRNA synergistically impact the protein output[5, 6]. To achieve enduring and efficient translation, the ORF sequence should be optimized towards more stable secondary structure without compromising its codon preference.

Recent advancement in circRNA demonstrated its potentials as next generation vaccines or therapeutics owing to its uniqueness in endless structure distinct from linear mRNA[7-9]. Other than ORF region, synthetic circRNA usually contains internal ribosome entry site (IRES) motif upstream of ORF for translation initiation[10]. The correct folding of IRES as a functional motif to recruit translation pre-initiation complex (PIC) is a prerequisite of efficient translation of circRNA[11]. However, due to the lack of structure prediction tool for circular RNA, along with insufficient understanding of the crosstalk between IRES and ORF regions on circRNA, current sequence optimization of circRNA heavily relied on modular screening[12]. This independent ORF optimization on circRNA without considering the backbone sequence including IRES motif and residual regions as a whole introduces more uncertainties in the process of circRNA sequence optimization.

Here we present an efficient approach called circDesign based on previously reported LinearDesign algorithm[6] to generate optimized circRNA sequences for rabies and VZV vaccine development. In brief, a pool of candidate ORFs were firstly generated using LinearDesign algorithm based on optimization of codon usage and minimum free energy (MFE). By assembly of ORF with IRES motif as well as other functional regions, the positional entropy and ensemble diversity were evaluated aside from overall MFE and codon adaptation index (CAI)[13-15]. To

evaluate the impact of these parameters on circRNA performance, we performed *in vitro* and *in vivo* characterization of these circRNAs compared to conventionally optimized ORF sequences, it demonstrated greater performance in terms of circularization, stability, protein translation as well as *in vivo* immune responses. The circDesign approach provides a general strategy for protein-coding circular RNA design and potentially enables broader circRNA-based vaccine and therapeutic development.

Results

circDesign approach for circular RNA design

To implement circDesign for circRNA-based rabies vaccine design, the ORF region encoding RABV-G[16, 17] was designed such as to achieve efficient and prolonged expression. Different from linear mRNA design which is composed of relatively short functional elements (~ 100 nt in length) including 5'-UTR and 3'-UTR, artificially constructed circular RNA with protein translation capacity usually contains long viral or cellular IRES sequence (500-800 nt in length) for cap-independent translation[10, 18, 19]. More importantly, the IRES region needs to be independently folded into a hierarchical structure without interference from other sequence as to efficiently recruit translational PIC. Therefore, a key consideration in circDesign involves mitigating the cross-interaction of ORF region with IRES motif, thus facilitating the formation of functional IRES with high confidence. Moreover, following a permuted intron-exon (PIE) circularization[20], residual exon fragments on circularized RNA is redundant and introduced more uncertainties to the function of circRNA as this element may interfere with the folding of other elements. As such, precautions must be taken when optimizing the ORF of circRNA since functional IRES motif and residual exons are present in the sequence.

In this study, the circDesign approach consisted of four integral steps as illustrated in **Fig. 1a**. In brief, the first step involves the implementation of LinearDesign algorithm to generate a pool of ORF candidates. Followed by the screening of ORF based on CAI and MFE, the stability and translation efficiency were carefully considered. Then a completed circular RNA was assembled with other necessary residual fragments including IRES, exons and spacers. In addition, the positional entropy of IRES and ensemble diversity of circRNA were evaluated. Lower positional entropy suggests a more conserved structure of IRES, while a lower ensemble diversity indicates a higher consistency and predictability of the circRNA structure, both of which contribute to higher structure stringency[21, 22]. In addition, the inter-region and intra-region interaction was evaluated primarily aiming to mitigate the impact from ORF on the independent folding of IRES, which is critical for efficient translation initiation. Based on the

abovementioned screening process, the designed circRNAs were then subjected to *in vitro* and *in vivo* evaluation for screening.

Design, synthesis, and characterization of circular RNA encoding RABV-G

Herewith RABV-G encoding circRNA, we designed six ORFs, along with two benchmark sequences. The six circDesign-generated designs are widely dispersed in the low-MFE regions (**Fig. 1b**). To better understand the impact of MFE and CAI in terms of biological implications, following the LinearDesign's experimental design principle, we crafted sequences with nearly identical values in MFE (CR2, CR3 // CR4, CR5) or in CAI (CR5, CR6, CR-Ther // CR1, CR2, CR-Novo). Benchmark ORF sequences (CR-Ther and CR-Novo) were designed with publicly available platforms from Thermo Fisher and Novoprotein respectively, which primarily optimized the codon preference without considering the secondary structure. The color darkness of each sequence represents the ensemble diversity of assembled circular RNA. As suggested, the ensemble diversity of designed circRNA is correlated with MFE. With a lower MFE of ORF region, the ensemble diversity of circRNA was lowered, suggesting a more well-defined structure with independent folding of each region.

To synthesize the circRNA, the circularization of RNA was mediated by self-cleaving permuted group I catalytic intron which was separated into 5'-intron and 3'-intron in the original sequence design as previously reported[7, 20]. In brief, both ends of linear mRNA consisted of complementary homology arms facilitating the folding of active ribozyme structure, thus undergoing two constitutive transesterification reactions to form junction between two exon fragments (E1 & E2). In this study, IRES from Coxsackievirus B3 (CVB3)[23, 24] was adopted upstream of open reading frame (ORF) to drive the protein translation process. As shown in the **Fig. 1b**, different ORF embedded in the linear mRNA design could be incorporated in circular RNA *via* the same circularization reaction. Taking CR3 and CR-Novo as representative sequences, the ORF of CR3 was designed with much lower MFE and less inter-region interaction with IRES motif compared to CR-Novo. As shown in **Fig. 1c**, though with the same backbone sequence and amino acid sequence, most of the amino acid could be coded by different synonymous codons, resulting in numerous sequence design space. The secondary structure of CR3 and CR-Novo was predicted as **Fig. 1d**. It was clear that the same IRES region (light grey color) had distinct folding in two circRNAs. The secondary structure folding prediction of circRNA rabies sequences (see **Extended Data. 1&2**) demonstrated that suboptimal ORFs (Ther and Novo) may disrupt the correct folding of IRES. And the pairwise visualization of these two circRNA (**Fig. 1e**) showed that CR-Novo had more inter-region base pairing (red connecting line) than that of CR3. The base pairing in CR3 mainly led to intra-region folding (blue connecting line).

194 Same results were obtained in other circDesign-based sequences (see **Extended**
195 **Data. 3&4**).
196
197 As a result of the difference in MFE, CAI value and ensemble diversity, the
198 circularization efficiency varied among these sequences. Considering a more
199 compact ORF region folding with less interference with the formation of active
200 intron, circDesign-generated sequences (CR1-6) had relatively higher
201 circularization efficiencies than those of CR-Novo and CR-Ther (**Fig. 2a**). To
202 remove impurities from the circularization reaction products, size-exclusion
203 column chromatography was used to obtain purified circRNA (see **Extended**
204 **Data. 5a**) which induced minimized innate immunogenicity (see **Extended Data.**
205 **5b-c**). To characterize the circRNA, non-denaturing agarose gel electrophoresis
206 was performed at room temperature. As shown in **Fig. 2b**, it's intriguing to find
207 that the gel mobility of circRNAs was well correlated with their MFE values
208 given their same nucleotide length. CR-Novo sequence, with the highest MFE,
209 exhibited the slowest mobility in the gel matrix possibly due to its less compact
210 structure, while circDesign-generated sequences especially CR1-5 had faster
211 migration as a result of their highly compact folding structure. This suggested the
212 potential of optimizing ORF sequences of circRNA in regulating their folding
213 paradigm.
214
215 **Optimized circRNA exhibited enhanced *in vitro* stability**
216
217 As the secondary structure dictates the functionally half-life of mRNA[5], we then
218 extensively evaluated the *in vitro* stability of circRNAs in terms of
219 thermodynamic folding, in-solution degradation as well as intracellular decay. By
220 heating the circRNA in solution to gradually unfold its structure, the fluorescence
221 intensity from RNA bound RiboGreen® reagent attenuated accordingly. We
222 calculated the melting temperature (T_m) of circRNA from the fluorescent intensity
223 curve as **Fig. 2c**. CR1-3 had slightly higher T_m than CR4-6, with an obviously
224 increased thermodynamic stability compared to CR-Novo and CR-Ther. The
225 melting curve results was associated with MFE values.
226
227 Like linear mRNA, the chemical instability of circRNA originated mainly from
228 hydrolysis reaction despite of its endless structure[25-27]. To examine the in-solution
229 stability of all circRNAs, RNA samples were incubated in PBS buffer containing
230 10 mM Mg^{2+} at 37 °C mimicking the physiological buffering system over a time
231 course of 60 h. At different time points, the integrity of circRNA was assessed.
232 The degradation of circRNA as a function of time was fitted to a one-phase decay
233 curve, suggesting different degradation kinetics. circRNAs with higher MFE
234 values (CR-Novo & CR-Ther) underwent faster degradation kinetics with
235 half-life ($t_{1/2}$) of 9.14h and 9.68h respectively, while CR1-3 had considerably
236 extended $t_{1/2}$ ranging from 15.56 to 20.62 h (**Fig. 2d**).

237
238 Apart from chemical degradation, the intracellular decay of exogenous circRNA
239 is also regulated by different pathways in related to its translational activity[28, 29].
240 To assess the in-cell half-life of circRNA, the abundance of circRNA extracted
241 from cells was quantified using reverse transcription quantitative real-time PCR
242 (RT-qPCR) method at various time points (3, 12, 24, 48 and 72h)
243 post-transfection into Human Skeletal Muscle Cells (HSkMC). As illustrated in
244 **Fig 2e**, a slightly different decay pattern of all tested circRNA was observed. CR1
245 and CR3 had a prolonged intracellular half-life (24.34 h and 19.31 h, respectively)
246 while CR-Novo and CR5 showed a faster in-cell decay (10.21 h and 9.18 h,
247 respectively). As the biological fate of transfected circRNA is associated with a
248 plethora of factors including translation status and nuclease resistance[30, 31], the
249 in-cell degradation of artificially synthesized circRNA could possibly be
250 controlled by tuning its secondary structure and translation efficiency. We
251 reasoned that CR3 sequence had decent stability in conjunction with high
252 translation efficiency, enabling its resistance against chemical degradation and
253 biological decay.
254
255 **circDesign improved the protein coding capacity of circRNA**
256 Since the stability and translation efficiency of circRNA co-regulates the protein
257 output level, we evaluated the RABV-G expression from transfected circRNA in
258 HSkMC using flow cytometry (**Fig. 2f**). To gain thorough comparison, we
259 included conventional chemically modified linear mRNA harboring Novo ORF
260 encoding RABV-G as a control group as well. At 24 h post-transfection, antigen
261 was highly expressed in CR3 group as suggested by the mean fluorescent
262 intensity (MFI). CR1-5 had a remarkably higher protein output level than CR6
263 and CR-Ther, largely attributed to the relatively instable structure of CR6 and
264 CR-Ther. However, it's interesting to find that benchmark CR-Novo exhibited a
265 decent protein coding capacity despite of its lower CAI value compared to
266 CR-Ther. This evidence emphasized the importance of taking multiple influential
267 factors into consideration other than CAI to stratify the mRNA coding potentials.
268 Moreover, we found that the circular form (CR-Novo) outcompeted its linear
269 counterpart (LR-Novo) in protein translation level (**Fig. 2f**), where stability factor
270 might be the major contributing factor as these two forms of RNA shared the
271 same CAI of ORF. The correlation analysis of in-solution and in-cell half-life
272 with MFE (**Fig. 2g**) showed the importance of MFE parameter in improving
273 circRNA half-life. Predicted half-life correlated well with the observed
274 experimental data (**Fig. 2h**).
275
276 To elucidate the underlying mechanism of enhanced protein expression in relation
277 to structure (**Fig. 3a&b**), we performed ribosome profiling[32] and polysome
278 profiling[33] analysis of CR3 and CR-Novo for side-by-side comparison. Following
279 the standard workflow (**Fig. 3c**) after transfection into cells, the ribosome

280 footprints were aligned to the full-length CR3 and CR-Novo, respectively. The
281 ultracentrifugation fractions were quantified to determine the fractional
282 composition of circRNA. In both RNA direct sequencing counts and ribosome
283 sequencing counts (**Fig. 3d**), the CR3 had higher fpkm (fragment per kilobase of
284 transcript per million mapped reads) of RNA-seq and ribo-seq than that of
285 CR-Novo at the time of cell being harvested, indicating a higher circRNA
286 abundance and ribosome footprints of CR3. Footprint abundance relative to
287 mRNA abundance dictates the TE (translation efficiency) [34] of circular RNA. The
288 TE of CR3 (233.7) was calculated as 1.5-fold of CR-Novo (159.9), suggesting a
289 markedly higher translation efficiency from circDesign optimized CR3. After
290 alignment of the ribosome footprints on circRNA, it's clear that the
291 cap-independent translation mechanism of circRNA driven by CVB3 IRES
292 efficiently recruits ribosome onto circular RNA to initiate the protein translation.
293 Most of the ribosome protected fragments were identified in ORF region in both
294 CR3 and CR-Novo, though the read count and distribution varied between these
295 two groups. As suggested in **Fig. 3e**, the ribosomal footprints were mapped and
296 distributed more evenly throughout the ORF region while CR-Novo had more
297 distinct footprint accumulation peaks. The fully aligned ribosomal footprints were
298 plotted on circular CR3 and CR-Novo annotated with each functional regions,
299 respectively (**Extended Data. 6**). In addition, several major peaks upstream of
300 ORF indicated the recruitment of ribosome for translation initiation. Taking a
301 closer look at the secondary structure and pairwise visualization (**Extended Data.
302 7**), it's highly possible that the disrupted IRES motif in CR-Novo impeded the
303 translational machinery recruitment, thus resulting in a much lower ribosome
304 footprint abundance.
305
306 In addition, polysome profiling was performed on CR3 and CR-Novo to compare
307 the ribosome loading capacity. Ultracentrifugation of both CR3 and CR-Novo
308 was successful as shown in **Fig. 3f**, which quantified the total RNA in each
309 fractional position. 80S fraction referred to monosome and later peaks referred to
310 polysome-bound circRNA. By further quantifying the CR3 or CR-Novo in each
311 collected fractions, we observed a higher ribosome loading in CR3 compared to
312 CR-Novo (**Fig. 3g**).
313
314 **LPP delivery system efficiently delivered circRNA *in vitro* and *in vivo***
315 To investigate the performance of circRNA *in vivo*, a proprietary lipopolyplex
316 (LPP) delivery system[35, 36] was used to formulate the circular RNA. As shown in
317 **Fig. 4a**, following a two-step microfluidic mixing process, cationic polymer
318 complexed circRNA could be encapsulated in a bilayer liposome-like
319 nanoparticle with a "core-shell" structure. Previous studies have demonstrated the
320 efficiency and safety of using this LPP delivery system to deliver linear mRNA[37,
321 38]. Herewith circRNA encoding GFP (CR-GFP) or firefly luciferase (CR-FLuc)
322 was formulated into LPP to study its *in vitro* cell expression and *in vivo*

323 biodistribution compared to its chemically modified linear counterpart (LR-GFP
324 or LR-FLuc), respectively. Flow cytometry analysis of cells treated with LPP
325 formulated CR-GFP showed a dosage-dependent translation from 50 ng, 200 ng
326 to 500 ng per well in a 6-well plate. Stronger expression was observed in circular
327 RNA group than that of LR-GFP (**Fig. 4b**). Besides, the protection of
328 encapsulated circRNA against RNase digestion was evaluated in LPP and lipid
329 nanoparticle (LNP), a widely used mRNA delivery system. The residual circRNA
330 was quantified at 30 min post-treatment and the results suggested a higher
331 protection efficacy against nuclease digestion using LPP formulation.
332
333 Upon intramuscular administration of LPP formulated CR-FLuc and LR-FLuc in
334 mice, *in vivo* imaging system (IVIS) captured the whole-body *in vivo*
335 luminescence activities at different time points (6, 24, 48, 72, 96 and 168 h) (**Fig.**
336 **4d**), reflecting the expression kinetics of luciferase from CR-FLuc or LR-FLuc. It
337 turned out that circular RNA produced luciferase in a more durable manner with
338 higher accumulated expression as shown in **Fig. 4e**. Though with similar
339 physicochemical properties of LPP formulation (**Extended Data. 8a**) and lower
340 onset expression as seen at 6 h post administration, CR-FLuc showed extended
341 expression over the course of one week while luminescence from LR-FLuc group
342 descended to background level within a relatively shorter time (2 days
343 post-dosing). A gross estimation of accumulated expression was conducted
344 simply by calculating the area-under-curve (AUC) of total flux of luminescence.
345 CR-FLuc group led to approximately 5.3-fold of total luciferase expression
346 compared to its linear counterpart over the course of 8 days (**Fig. 4f**). Indeed,
347 other group has reported similar translation kinetics of circular RNA compared to
348 linear mRNA[12], thus rendering circRNA a promising therapeutic or vaccine
349 platform for sustained protein supplement or enduring protection against
350 pathogens. These results suggested the feasibility of using LPP for efficient *in*
351 *vivo* delivery of circRNA despite of its closed loop feature.
352
353 **circDesign optimized circRNA rabies vaccine demonstrated superior *in vitro***
354 **stability and *in vivo* performance**
355
356 It has been reported that linear mRNA encapsulated in lipid nanoparticles still
357 underwent slow transesterification hydrolysis[25]. In this study, the stability of
358 LPP-circRNA nanoparticles was evaluated to simulate the vaccine storage
359 condition under the formulated situation. Henceforth, the same lipid composition
360 was adopted to encapsulate circDesign-optimized CR1-6 and benchmark
361 circRNA encoding RABV-G to rule out the impact from delivery system on their
362 *in vitro* and *in vivo* performance. The *in vitro* characterization of formulated
363 circRNAs showed that LPP nanoparticles had similar size of around 110 nm (**Fig.**
364 **4g**) and positive zeta potentials (in the range of 20-35 mV) (**Fig. 4h**) regardless of
365 the encapsulated circRNA. However, the importance of optimizing the stability of

366 circRNAs was manifested in their storage stability in lipid formulation. We
367 examined the mRNA content of LPP-circRNA complex on day 30 at room
368 temperature to assess the integrity of RNA component. A faster RNA degradation
369 in LPP formulated CR-Novo and CR-Ther was observed (**Fig. 4i**) with 15-20%
370 circRNA loss on day 30 while circDesign optimized circRNAs (CR1-5) showed
371 little degradation over tested period. Moreover, the in vitro innate
372 immunogenicity and cell cytotoxicity was evaluated with LPP formulated
373 circRNAs compared to linear RNA (**Extended Data. 8b&c**). Minimal *in vitro*
374 innate immunogenicity and cell toxicity was observed for SEC purified circRNAs
375 formulated by LPP.
376
377 We then evaluated the *in vivo* immunogenicity of RABV-G encoded RNA
378 vaccines. By intramuscular injection into mice, it's proposed that the
379 circRNA-LPP nanoparticles entered antigen-presenting cells *via* endocytic
380 pathway and circRNA got released from endosome into cytoplasm for antigen
381 translation. The translated antigens were then processed to elicit humoral and
382 cellular immune responses as illustrated in **Fig. 5a**. Two doses of rabies vaccines
383 were *i.m.* administered at an interval of two weeks in balb/c mice (n=5 per group).
384 Mice were weighted after first dosing and no weight loss was observed for both
385 circRNA and linear RNA group (**Extended Data. 8d**). Mice sera were collected
386 on day 10, 14, 21 & 28 to assess the pseudovirus neutralizing antibody titer
387 (pVNT) and spleens were extracted for cellular immunity assessment on day 28
388 (**Fig. 5a**). As neutralizing antibodies (nAbs) play a critical role in protection
389 against rabies virus[39], monitoring the geometric titer (GMT) nAb level gave us a
390 hint on the efficacy of rabies vaccines. In this study, linear mRNA encoding the
391 same ORF (LR-Novo) as CR-Novo was used for comparison as well. On day 10
392 post-priming dose, LR-Novo elicited a slightly higher antibody titer compared to
393 all circRNA groups possibly due to relatively faster onset expression of antigens,
394 though overall titers remained low (**Fig. 5b**). Slower but durable antigen
395 expression induced comparable immune responses among circRNA groups while
396 CR1, with the lowest MFE, had 2-fold pVNT of LR-Novo and 4-fold pVNT of
397 CR-Novo (**Fig.5c**). One week after booster (day 21), circDesign-optimized
398 sequence groups (CR1-4) elicited much stronger humoral immune responses than
399 the rest of groups (CR5-6, CR-Novo, CR-Ther and LR-Novo) (**Fig. 5d**). Of note,
400 all circular RNA groups exhibited continued increase in pVNTs on day 28,
401 whereas linear RNA had no further enhancement in antibody titer (**Fig. 5e**). The
402 geometric increase (GMI) of pVNT was calculated based on the GMT on day 10
403 as baseline to show the trend of humoral immune response induction. As plotted
404 in **Fig. 5f**, LR-Novo had the least GMI trend while CR1&3 showed durable
405 induction of immune responses. The pVNT kinetics of each group as a function of
406 time were summarized as **Fig. 5h**, suggesting the great potentials of
407 circDesign-enabled vaccine design in triggering strong antibody responses. It's
408 worth noting that cellular immune responses induced by circDesign optimized

409 sequences (CR1-4) especially CR3 are more prominent than other groups (**Fig.**
410 **5g**). A higher frequency of RABV-G specific T cells secreting interferon γ (IFN-γ)
411 was observed in CR3 group with a mean value of 280.1 spots counted using
412 Enzyme-linked immunosorbent spot (ELISpot) assay (**Extended Data. 9**).
413 Though the practical significance of higher RABV-G specific cellular immunity
414 in rabies prevention remains elusive[40, 41], we speculate the improved T cell
415 immune responses from circDesign optimized vaccine may play important roles
416 in rabies virus clearance from the host[40]. Taking a closer look at the cellular
417 immune activation profile, flow cytometry analysis of the RABV-G peptide
418 stimulated T cells was performed. Following a stepwise gating of the cell
419 population (**Extended Data. 10**), the ratio of $CD4^+$ and $CD8^+$ T cells producing
420 IFN-γ, TNF-α, IL-2 and IL-4 were computed, respectively. The results indicated
421 the strong RABV-G specific $CD4^+$ and $CD8^+$ T cell responses elicited by
422 circDesign generated vaccines (**Extended Data. 11**). We observed higher ratios
423 of IFN-γ, TNF-α and IL-2 secreting T cells but minimal IL-4 producing
424 population in both $CD4^+$ and $CD8^+$ T cells (**Extended Data. 11**), suggesting a
425 T_h1-biased immune responses induced by circRNA rabies vaccines.
426
427 Combined with the in-solution and in-cell stability results of naked or LPP
428 formulated circRNA, these results convincingly demonstrated the improved
429 potency from circDesign-optimized sequences owing to their well-defined
430 structure and enhanced stability during storage and intracellular trafficking. The
431 correlation analysis of *in vivo* pVNT and ELISpot on day 28 showed the relation
432 to MFE of circRNA (**Extended Data. 12**).
433
434 **The durable humoral immune response may be related to the *in vivo* stability**
435 **of CR3**
436
437 The abovementioned *in vitro* and *in vivo* evaluation of circRNAs implicated the
438 importance of circRNA stability as well as translation efficiency in achieving
439 optimal performance. Therefore, balancing the optimization of CAI (translation
440 efficiency) and MFE (stability) with a well-defined circRNA folding structure
441 might synergistically contribute to a top performer sequence, thus leading to
442 maximized *in vivo* outcomes. Of all circDesign optimized sequences, CR3
443 showed superior stability, protein translation output, along with *in vivo*
444 immunogenicity (See **Extended Data Table 1** for summarized assessment
445 results). Compared to CR-Novo, it's intriguing to find that another benchmark
446 sequence CR-Ther had lower protein translation and induced relatively weaker
447 immune responses despite its higher CAI. Consequently, we further compared
448 CR-Novo with CR3 regarding their *in vivo* stability to explain the advantages of
449 circDesign-generated CR3 over CR-Novo in their potency and durability. To
450 study the *in vivo* stability, LPP formulated CR3 and CR-Novo were *i.m.*
451 administered into balb/c mice (n=5 per group). At 6, 24, 48, 72 and 168 h

452 post-dosing, mice were sacrificed and total RNAs were extracted from different
453 organs including muscle (injection site), lymph node, spleen, liver, lung, heart,
454 kidney, brain and small intestine (sm. int.). A standard plasmid containing the
455 target sequence was used as internal standard control to quantify the circRNA
456 copies per μg of total RNA using qPCR analysis. The biodistribution results
457 revealed the good safety profile of LPP delivery system, as major injected dose
458 accumulated at the injection site without significant retention in liver both for
459 CR3 (**Fig. 6b**) and CR-Novo (**Fig. 6a**). Moreover, as time went by, more fractions
460 of circRNA were detected in spleen and lymph node where the immune activation
461 mainly occurs. It's noted that CR3 had extended muscle retention proportion
462 (88.5%, 70% and 29.4% at 24h, 48h and 72h, respectively) compared to CR-Novo
463 (74.5%, 25.4% and 7.4% at 24h, 48h and 72h, respectively) (**Fig. 6c**). The
464 comprehensive quantification data were summarized in **Extended Data Table 2**.
465 It's hypothesized that higher *in vivo* stability of CR3 benefited the longer retention
466 at injection site given the same dosage as CR-Novo. Within 72 h of administration,
467 the circRNA quantification data of muscle at injection site suggested the higher
468 abundance of CR3 (**Fig. 6d**). This potentially contributed to a sustained lymphatic
469 migration of antigen presenting cells (APCs) to peripheral immune organs such as
470 draining lymph nodes and spleen, leading to robust immune activation.
471
472 **The long-lasting humoral immune response induced by circDesign**
473 **optimized rabies vaccine**
474
475 Above findings rendered CR3-LPP a more potent rabies vaccine candidate
476 potentially inducing long-lasting adaptive immunity against rabies virus. To study
477 the longevity of immune responses, balb/c mice (n=5 per group) were immunized
478 with LPP formulated CR3 and CR-Novo with the same dosage (2 μg per
479 immunization for prime and boost at an interval of two weeks). The mice sera
480 were collected over a much longer period during which the nAb titer was
481 monitored (**Fig. 6e**). As shown in **Fig. 6f**, CR3 induced a stronger humoral immune
482 response following prime and booster. 14 days after booster dose (on day 35), the
483 pVNT of CR3 group remained 1.7-fold of CR-Novo (**Fig. 6f**). With a relatively
484 slower waning rate of pVNT, CR3 group exhibited 2.1-fold and 3.2-fold pVNT
485 over CR-Novo group on day 90 and 163, respectively. According to the
486 guidelines of rabies vaccine released by World Health Organization (WHO), a
487 second booster was recommended when re-exposure to rabies virus occurred 3
488 months after the last booster[42]. Thus, we administered the second booster in mice
489 on day 163 to evaluate the immune responses after re-boost. The second booster
490 induced much stronger immune response in CR3 group with 4.6-fold and 3.9-fold
491 pVNT of CR-Novo one week (day 170) and two weeks (day 177) after re-booster dose
492 (**Fig. 6f**). Besides, the cellular immune responses were assessed by ELISpot on
493 day 170 using mice spleenocytes. CR3 immunized mice had shown significantly
494 stronger antigen-specific IFN-γ and TNF-α secretion, potentially leading to better

clinic outcome.

Second antigen demonstrating the robustness of circDesign in optimizing circRNA for improved performance

The *in vitro* and *in vivo* results of circRNA encoding RABV-G demonstrated the usefulness of circDesign algorithm in circular RNA sequence design. Considering the potential applicability of circDesign for different circRNA design and optimization, we validated the robustness of this algorithm using varicella-zoster virus (VZV) glycoprotein E (gE) as a second antigen to develop circRNA-based vaccine. At the same time, a new self-cleaving ribozyme from *Azoarcus* pre-tRNA was adopted to mediate the circularization reaction (See Supplementary materials for sequence details).

Though with a different intron splicing, the circularization of circRNAs harboring circDesign optimized VZV gE sequences was still highly efficient. In this comparison, we included three control sequences: CV-Poka which stems from a CAI-maximized sequence (CAI = 1); CV-Ther from a public optimization tool supported by Thermo Fisher; CV-Ori refers to the original wild-type VZV strain sequence without optimization (**Extended Data Fig. 13a**). Non-denaturing agarose gel electrophoresis of circRNAs showed similar correlation of migration rate with structural compactness (**Extended Data Fig. 13b**). Circularization efficiency, thermodynamic stability and in-solution stability analysis of all circRNAs encoding VZV gE revealed a good correlation with MFE value and ensemble structure diversity (**Extended Data Fig. 13c,d&e**). As revealed by the secondary structure prediction and pairwise visualization (**Extended Data Fig. 14-17**), CV1-5 had well-defined structure and less IRES folding interruption. The protein translation level assessed by flow cytometry indicated the importance of stability factor in durable protein expression, highlighted by the MFI at 48 h post-transfection into HSkMC cells (**Extended Data Fig. 13f**). Furthermore, the *in vivo* immune responses triggered by LPP formulated circRNA VZV vaccines were evaluated in balb/c mice (n=5). CV1-5 elicited significantly higher binding antibody titers than benchmark circRNAs on day 21 and 28 (**Extended Data Fig. 18**). It was noteworthy that CV-Poka had compromised *in vitro* and *in vivo* performance despite of a maximized codon preference, in that its susceptibility to degradation as a result of high MFE value. Studies have suggested that eliciting a strong cellular mediated immune response is a key determinant for the vaccine protective efficacy against herpes zoster[43]. Therefore, we assessed the cellular immune response using ELIspot. It was inspiring to find that circDesign optimized sequences CV1-5 induced stronger VZV gE-specific T cells, which is a key determinant of VZV vaccine efficacy (**Extended Data Fig. 18d**).

Taken together, we successfully exploited the circDesign on the design of second

538 antigen and validated the outstanding design strategy *in vitro* and *in vivo*.
539

540 Discussions

541

542 In this study, we devised a novel algorithm tool, called circDesign, for simplified
543 circular RNA design to improve its stability as well as translatability. The
544 usefulness of this circDesign platform was validated using RABV-G and VZV gE
545 antigens against the benchmark designs which were designed via conventional
546 CAI-oriented method. Here we present evidence supporting the enhanced
547 stability and translation efficiency of circDesign optimized sequence which
548 contributed to considerably stronger in vivo immune responses. We speculated
549 that the sustained expression of antigens at high efficiency achieved greater
550 antigen-specific immune activations, leading to distinguished vaccine-elicited
551 humoral and cellular immune responses. Overall, these data demonstrated an
552 approach for rational circRNA design in support of next generation vaccine and
553 therapeutic development.
554

555 The major limitation of this study lies in the fact that we performed extensive
556 search on specific ORF sequences without further optimization of other
557 functional regions of circRNA such as IRES motif. To the best of our knowledge,
558 the de novo design of an efficient IRES motif remains challenging as these virally
559 or cellularly derived IRES motifs are usually sensitive to sequence manipulation
560 including deletion, mutation, or insertion. The different domains of IRES
561 sequence cohesively function to recruit PIC and assemble the intact ribosome
562 complex only when these domains are well-folded. Therefore, we did not
563 incorporate the modulation of IRES region in the circDesign at current stage.
564 Provided that the structure-to-activity of IRES were elucidated at molecular level,
565 it might be possible to realized bottom-up search or optimization of IRES
566 sequence in circDesign algorithm.
567

568 Other than IRES-driven translation from circRNA, N6-methyladenosine (m6A)
569 modification upstream of ORF has been reported to facilitate the translation as
570 well as the stability[44, 45]. If chemically modified nucleotides were incorporated
571 into circRNA, it would pose difficulties on our circDesign algorithm as the
572 structure prediction based on unmodified nucleotides is not reliable. Given that
573 the energy model of chemically modified nucleotide is available, we would be
574 able to do extensive structure comparison for optimal sequence design.
575

576 Materials & Methods

577 ***Ensemble diversity calculation***

578 Ensemble diversity (ED) measures the complexity of the structural ensemble,
579 which can be computed from pair probabilities.

$$\mathrm{ED} = \sum_{i,j} p_{ij} \times (1 - p_{ij})$$

Positional entropy calculation

Positional entropy (PE) is a metric that measures whether a specific nucleotide at position *k* predominantly occurs in the same configuration, paired or unpaired.

$$\mathrm{PE}(k) = -\sum_{i} p_{ik} \ln p_{ik}$$

Positional entropy of the IRES region is defined as:

$\mathrm{PE(IRES)} = \sum_k \mathrm{PE}(k)$, where *k* is in the region of IRES. The positional entropy is 0 for a nucleotide that is always unpaired or always paired with the same partner. Thus, positions with low entropy are predicted with high confidence.

circRNA secondary structure prediction

The circRNA secondary structure was modeled by ViennaRNA[46] with parameters for circular (-p -d2 -c) RNAs. And the structure was visualized by RiboGraphViz with the cirRNA secondary structure from RNAfold.

Vector and plasmid construction

To construct a vector for circRNA synthesis, T7 promoter, homology arm, elements from permuted intron-exon (PIE) construct, spacer, IRES, and coding sequences were synthesized by General Biol and cloned into pUC57-mini plasmid. For linear RNA synthesis, the pUC57 plasmid vector containing T7 promoter, 5' UTR, Kozak sequence, coding region, 3' UTR and polyA tail was synthesized by General Biol. All the sequences coding Firefly Luciferase (FLuc), RABV-G and VZV-gE are supplied in supplemental materials.

Plasmid DNA synthesis and linearization

pDNA was transformed into *E. coli* (Tsingke Biotechnology) and cultured in 100 mL of Luria Broth (LB) with 100 mg/mL Ampicillin (Sangon Biotech, CN). Plasmid was purified using a NucleoBond Xtra Midi kit (MN) and the concentration and purity was measured on a NanoDrop One (Thermo Fisher). pDNA was linearized using SapI restriction enzyme for 3 h at 37 °C and purified as template. After sequencing verification, the products were stored at -20 °C and were used as templates for *in vitro* transcription (IVT).

In vitro transcription and circularization of RNA

For the chemically modified linear mRNA synthesis, *in vitro* transcription reaction with 100% N1-methylpseudouridine (Hongene Biotech) substitution was

618 conducted at 30 °C for 16 hours. mRNA was co-transcriptionally capped using
619 m7(3'OMeG)(5')ppp(5')(2'OMeA)pG capping reagent (Hongene Biotech) in a
620 "one-pot" reaction followed by digestion with DNase I (Thermo Fisher). Linear
621 mRNA was purified using Dynabeads MyOne Carboxylic Acid beads (Thermo
622 Fisher).
623
624 For the circular RNA synthesis, The linear RNA precursor transcripts were
625 produced using 1 μg of linearized DNA template in a MEGAScript™ reaction
626 (Ambion) for 16 h at 30 °C, according to the manufacturer's protocol. Then RNA
627 was treated with DNase I (Thermo Fisher) for 60 min at 30 °C, followed by
628 lithium chloride precipitation. To obtain circularized RNA, GTP was added to a
629 final concentration of 2 mM along with a buffer including magnesium (50 mM
630 Tris-HCl, (pH 8.0), 10 mM $MgCl_2$, 1 mM DTT; Thermo Fisher). RNA was then
631 heated to 55 °C and held for 45 min before purification using Dynabeads MyOne
632 Carboxylic Acid beads (Thermo Fisher).
633
634 ***Liquid chromatography purification of circRNA***
635 Circular RNA products were further purified *via* liquid chromatography to
636 remove spliced introns and precursor linear mRNA using a 21.2×300 mm
637 size-exclusion column (SEC) with a particle size of 5 μm and pore size of 1000 Å
638 (Sepax Technologies). RNA was run on an AKTA avant 150 purifier system in
639 RNase-free 150 mM phosphate buffer (pH = 6.0). Purified circRNA products
640 were concentrated by lithium chloride precipitation and analyzed using Agilent
641 2100 bioanalyzer.
642
643 ***CircRNA sequence identification***
644 To validate the circularization of RNA, the SEC purified RNA was reverse
645 transcribed into cDNA using a HiScript III All-in-one RT SuperMix Perfect kit
646 (Vazyme), followed by PCR with primers that can amplify transcripts across the
647 splicing junction site. The PCR products were sequenced using Sanger
648 sequencing to validate the back-splicing junction of the circular RNA.
649
650 ***Circularization efficiency comparison***
651 To compare the circularization efficiency after circularizing reaction before SEC
652 purification, two sets of primers were used in qPCR method. One set of primers
653 was designed at 3 'intron, representing the part of RNAs that without successful
654 circularization ; the other set of primers was designed at the junction site,
655 representing the circRNAs formed by successful circularization. Therefore, the
656 circularization efficiency of different RNAs was obtained by comparison, and the
657 sequence of primers was as follows：
658 circ-Rabies-F (5'-3'): ACAAACGGCTATTATGCGTTACC;
659 circ-Rabies-R (5'-3'): GACTTGAACCCACACGACCG;
660 Linear-Rabies-F (5'-3'):AACGTCAAGACGAGGGTAAAGAGAG

661 Linear-Rabies-R (5'-3'):GACTTGAACCCACACGACC
662 circ-VZV-F (5'-3'): TAGCTCATGCTTGGTTAGAGCAG;
663 circ-VZV-R (5'-3'): CCCCCTGGGAGTCGAACC;
664 Linear-VZV-F (5'-3'):CGGCACCCACCTAAGGCAAAC;
665 Linear-VZV-R (5'-3'):CGAACCCAGCACCAACGGATTC;
666 To calculate the Circularization efficiency of each sequence:

667 $$\frac{\text{power}[2, -(x-y)] \times 100\%}{\text{power}[2, -(x-y)]+1}$$

668
669 x: Ct of circular RNA, y: Ct of linear RNA
670
671 ***Cell culture & circRNA transfection***
672 Human embryonic kidney 293 (HEK293, ATCC)/Human Skeletal Muscle Cells
673 (HSkMC, ATCC) and Baby hamster kidney 21 (BHK-21, ATCC) were cultured
674 in complete Dulbecco's Modified Eagle's Medium (DMEM, Gibco) containing
675 10% fetal bovine serum (FBS, Gibco) and 1% penicillin-streptomycin (Thermo
676 Fisher). Cells were seeded in a 6-well plate at a density of 5×10^6 cells/well 24 h
677 prior to transfection. Lipofectamine Messenger MAX (Thermo Fisher) was used
678 according to the manufacturer's instructions for the transfection of circRNA.
679
680 ***Agarose gel electrophoresis of circRNA***
681 To study the electrophoretic mobility profile of circRNA, RNA samples
682 suspended in Ambion® RNA storage buffer (Thermo Fisher) were denatured at
683 75 °C for 5 minutes and snap –cooled on ice before loaded onto 1% agrose gel
684 (130 V for 1 h at room temperature). DL5000 DNA marker (Vazyme) was used in
685 the gel. Gel image was taken by Gel Doc XR+ Gel Documentation System
686 (Bio-Rad).
687
688 ***In-solution stability assay of circRNA***
689 To assess the In-solution stability of mRNA, samples were incubated in PBS
690 buffer containing 10 mM Mg^{2+} . Sampling was conducted at different time points
691 (0, 1, 2, 4, 8, 12, 16, 24, 32, 48 and 60 hours). RNA integrity was analyzed by
692 Qsep100™ Capillary Electrophoresis System (BiOptic Inc). The integrity was
693 represented as the proportion of full-length mRNA calculated on
694 electropherogram. The data were normalized to time point 0 h.
695 To extrapolate the half-life of each sequence, one-phase decay equation:

696 $$Y = (Y_0 - \text{Plateau}) \cdot e^{-KX} + \text{Plateau}$$

697 was used to fit the curve. The Y_0 and Plateau were set as 100 and 0, respectively.
698 Half-life was computed as ln(2)/K, where K refers to decay rate constant.
699
700 ***Thermodynamic stability assay of circular RNA***
701 Equal volume of circRNA (1mg/mL) and diluted Quant-iT™ RiboGreen®

(Thermo Fisher) reagent was mixed in 1× TE buffer. A total of 20 μL mixture was loaded into 384-well plate and centrifuged at 1000 rpm for 1 min before running the Melting Curve program on QuantStudio 5 Real-Time PCR System (Applied Biosystems). circRNA underwent a denaturing process at 95°C for 5 min with a ramp rate of 0.05°C/s starting from 25°C. Then the temperature stepped down to 25°C with a rate of 1.6°C/s for annealing. The fluorescent intensity data at different temperatures were normalized to the initial value and plotted in GraphPad Prism 10.0. Sigmoidal curve was used to fit the data to extrapolate the melting temperature (T_m) of each circRNA.

In-cell stability assay of circular RNA

HSkMC cells were seeded in a 6-well plate at a density of 5×10^6 cells per well 24 h prior to transfection. Lipofectamine Messenger MAX (Thermo Fisher Scientific) was used according to the manufacturer's instructions for the transfection of circRNA. Cells were collected and and RNA was harvested and purified at 3, 12, 24, 48 and 72 h after transfection using an RNeasy Mini Plus kit (QIAGEN). Synthesis of first-strand cDNA from total RNA was performed with HiScript® III All-in-one RT SuperMix Perfect for qPCR (Vazyme). Gene specific TaqMan primers (TsingKe) amplifying the circRNA junction site were synthesized as below:

circ-tzF (5'-3'): ACAAACGGCTATTATGCGTTACC;

circ-tzR (5'-3'): GACTTGAACCCACACGACCG;

circ-Probe (5'-3'): FAM-ACGGACTTAAAATCCGTTGAC-MGB

Target amplification sequence was inserted into plasmid as an internal standard to obtain the absolute circRNA copies from RNA extracts. The qPCR reaction was carried out using Probe qPCR Mix kit (Takara) . For each sample, threshold cycle values (Ct) were processed according to the comparative Ct method. Gene expression levels were presented relative to Standard curve.

In vitro innate immunogenicity assay

24 hours post transfection of circRNA into C2C12 cells (ATCC), cell culture supernatant was collected. Interferon Beta level in supernatant was assayed by VeriKine TM Mouse IFN Beta ELISA Kit (PBL assay science) according to manufacurer's instruction. Optical density (OD) was measured at 450 nm using Bio-Tek Synergy I plate reader. The concentration of IFN-β was deduced from the standard curve.

Flow cytometry

24 hours post transfection of circRNA, HSkMC cells were harvested and resuspended in 1 mL of PBS buffer at a concentration of 1×10^7 cells/mL. 100 μL of the resuspended cells was added to a FACS tube and stained with 100 μL of Live/Dead Fixable Aqua Dead Cell Stain (Thermo Fisher Scientific) at a 1:100 dilution and human FcR blocking reagent (Miltenyi Biotec) at a 1:20 dilution on

745 ice for 30 min. Cells were then washed with 2.5 mL of FACS buffer and
746 centrifuged at 1500 rpm for 5 min. After centrifugation, cells were stained with 1
747 μg (1:100 dilution) of a anti-Rabies Virus CVS-11 antibody (Merck) or anti-VZV
748 gE mouse antibody (Abcam) at 4 °C for 30 min in dark before washing with 2.5
749 mL of FACS buffer and centrifuging at 1500 rpm for 5 min. Cells were then
750 stained with 100 μL of Goat PE-anti-mouse IgG (1:100 dilution) (Abcam) at 4 °C
751 for 30 min in dark. After incubation, cells were washed with 2.5 mL of FACS
752 buffer, centrifuged at 1500 rpm for 5 min and resuspended with 250 μL of PBS.
753 Samples were analyzed on BD Canto II (BD Biosciences). Data were processed
754 using FlowJo V10.1 (Tree Star).
755
756 ***RNA sequencing and ribosome profiling of circular RNA***
757 At 6 h post-transfection of CR-Novo and CR3 into HEK293 cells, cycloheximide
758 (Sigma) was added to cell culture medium to a final concentration of 100 μg/ml to
759 arrest protein synthesis and preserve ribosome-mRNA interaction. After a 2- min
760 incubation at 4 °C and lysis, the cell lysate was centrifuged at 3,000×g and the
761 supernatant containing free polysomes was decanted. To prepare ribosome
762 footprints (RFs), RNase I (NEB) and DNase I (NEB) were added to lysate and
763 was then incubated at room temperature on a Nutator mixer. Nuclease digestion
764 was stopped by adding SUPERase·In RNase inhibitor (Ambion)followed by
765 purification using size exclusion columns (GE Healthcare). Next, 10% (wt/vol)
766 SDS was added to the elution, and RFs with a size greater than 17nt was isolated
767 according to the RNA Clean and Concentrator-25 kit (Zymo Research). After
768 obtaining ribosome footprints, Ribo-seq libraries were constructed using
769 NEBNext® Multiple Small RNA Library Prep Set for Illumina® (catalog
770 no.E7300S, E7300L). Briefly, adapters were added to both ends of RFs, followed
771 by reverse transcription and PCR amplification. The 140-160bp size PCR
772 products were enriched to generate a cDNA library and sequenced using Illumina
773 HiSeqTM X10 by Gene Denovo Biotechnology Co. (Guangzhou, China).
774
775 ***Ribosome footprint data processing and alignment***
776 Low quality reads were filtered by fastp. Raw reads containing over 50% of
777 low-quality bases or over 10% of N bases were removed. Adapter sequences were
778 trimmed. Reads with length between 20-40 bp were retained for subsequent
779 analysis. Short reads alignment tool Bowtie2 was used for mapping reads to
780 ribosome RNA (rRNA) database, GenBank, Rfam database. The reads mapped to
781 rRNAs, transfer RNAs (tRNA), small nuclear RNAs (snRNA), small nucleolar
782 RNAs (snoRNA), and miRNA were removed. Processed RNA-seq reads were
783 aligned to the circular RNA using sequence alignment by STAR with 2-pass
784 setting enabled. The reads were assigned to different functional regions (IRES,
785 CDS, spacer, homology arm and exon) based on the position of the alignment.
786 Translation efficiency (TE) was calculated as the base 2 logarithmic ratio of
787 normalized RPFs over the normalized input for each ORF.

788

789 ***Pause sites analysis***

790 Because the translocation of ribosomes occurs along the mRNA one codon at a
791 time, the potential of single-codon resolution pauses were investigated. Using
792 PausePred (https://pausepred.ucc.ie/) which infers the locations of ribosome
793 pauses, global single codon pauses were analyzed.

794

795 ***Quantification of read abundance***

796 Reads counts in the different regions of circular RNA was calculated by software
797 RSEM, and the level was normalized by using FPKM (fragment per kilobase of
798 transcript per million mapped reads) method, and the formula is shown as
799 follows:

800 $$FPKM = 10^6C/(NL/10^3)$$

801 Given FPKM (A) to be the abundance of sequence A, C to be number of
802 fragments mapped to sequence A, N to be total number of fragments that mapped
803 to reference sequences, and L to be number of bases on sequence A. Therefore,
804 the calculated FPKM can be directly used for comparing the difference of
805 abundance among samples. The ribosome footprint depth was plotted in a circular
806 form with each functional region denoted in different color.

807

808 ***Polysome profiling of circRNA***

809 At 6 h post-transfection of CR-Novo and CR3 into HEK293 cells, cycloheximide
810 (Sigma) was added to cell culture medium to a final concentration of 100 μg/ml to
811 arrest protein synthesis and preserve ribosome-mRNA interaction, and the cells
812 were incubated at 37 ° C for 15 minutes. After trypsin digestion (0.25%), harvest
813 and wash cells with ice-cold PBS supplemented with 100 mg/mL cycloheximide.
814 The frozen tubes were flash frozen in liquid nitrogen and then stored at -80℃ for
815 later use. Samples were sent to NKY-GuangZhou Gene reader Bio-Medical
816 Technologies Co., Ltd. (Guangzhou, China) for isolation. In brief, cells were
817 lysed in lysis buffer (10 mM Tris-HCl pH 7.4, 150 mM NaCl, 5 mM $MgCl_2$, 1%
818 Triton X-100, 0.5% deoxycholate, 2 mM DTT) supplemented with 4 U/mL
819 RNase inhibitor, 100 μg/mL cycloheximide, and proteinase inhibitor cocktail
820 (Roche, Basel, Switzerland) on ice for 20 min. After centrifugation at 13,000 g for
821 10 min, the supernatant was then taken and loaded into a 10% to 45% sucrose
822 gradient solution and centrifuged at 360000 rpm for 3 h (Beckman Optima
823 XE-100). 18 fractions from each sample were collected using a piston gradient
824 fractionator (Biocomp, Fredericton, Canada) equipped with a Bio-Rad Econo UV
825 monitor, followed by total RNA extraction from each fraction for RT-qPCR
826 analysis.

827

828 ***Preparation of LPP-circRNA***

829 LPP nanoparticles were prepared by a two-step method as previously described[35].
830 Briefly, a cationic polymer compound (PbAE) was dissolved in PBS buffer
831 solution (pH=5.2) and circRNA was diluted with citrate buffer（pH4, 5 mM）and
832 RNase-free water. mRNA/PbAE complexes were prepared by a microfluidic
833 mixer (Inano D, Micro&Nano Technology Inc, China) at a volume ratio of 5:1
834 (mRNA: PbAE). After that, lipids were dissolved in ethanol at molar ratios of
835 40:15:43.5:1.5 (ionizable lipid: 1,2-dioleoyl-sn-glycero-3-phosphoethanolamine
836 (DOPE):Cholesterol: PEG-lipid). The lipid mixture was combined with
837 mRNA/PbAE complexes at a ratio of 3:1 (aqueous: ethanol) using a microfluidic
838 mixer. Formulations were concentrated using Amicon ultra centrifugal filters
839 (EMD Millipore) in sodium acetate with 10% sucrose buffer, passed through a
840 0.22-mm filter, and stored at 4℃.
841
842 ***Nanoparticle characterization***
843 The size, polydispersity index (PDI) and zeta potential of LPP formulated
844 circRNA were measured by dynamic light scattering (DLS) (Malvern, Zetasizer
845 Nano ZS). Briefly, LPP-circRNA samples were diluted in sodium acetate with
846 10% sucrose buffer at a concentration of 0.1 mg/mL. The measurement was
847 performed in triplicate with 8 runs in each measurement.
848
849 ***In vitro storage stability assay of LPP formulated circRNA***
850 LPP formulated circRNA was stored in sodium acetate with 10% sucrose buffer
851 at 4°C over a time course of 60 days. At Day 0, 30 & 60, LPP-circRNA was
852 sampled for physicochemical characterization including mRNA content,
853 hydrodynamic size and PDI.
854
855 ***Cell count Kit-8 (CCK-8) assay of LPP formulated circRNA***
856 Cell proliferation capacity was evaluated using CCK-8 assay kit (Sigma Aldrich)
857 according to the manufacturer's instructions. Briefly, HSkMC cells were seeded
858 into 96-well plates at a density of 5×10^5 cells/well. On the other day, 100 ng of
859 LPP formulated circRNA was added into cell culture directly. At 48 h
860 post-transfection, 10 μL CCK-8 solution was added to each well and cells were
861 incubated for a further 2 h at 37 °C. Optical density (OD) was measured at 450 nm
862 using Bio-Tek Synergy I plate reader.
863
864 ***mRNA concentration and encapsulation efficiency of LPP-mRNA***
865 LPP formulated circRNA was diluted with 1×TE buffer followed by mixing with
866 an equal volume of 2% Triton X-100 and incubated at RT for 20 min to release the
867 encapsulated mRNA-circRNA core. 100 μL of each sample was then transferred
868 to the wells of a 96-well plate, to which 100 μL of 200 × diluted RiboGreen™
869 RNA Reagent (Thermo Scientific) was added. The plate was shaken and
870 incubated at RT for 10 min. After that, the fluorescence of the plate was read by a
871 Bio-Tek Synergy I plate reader (BioTek). A series of diluted standards were also

872 prepared corresponding to 0.1–2.0 μg/mL mRNA. A standard curve of
873 fluorescence as a function of mRNA concentration was plotted by linear
874 regression, from which the mRNA concentrations of the samples were calculated.
875 Encapsulation efficiency was calculated as Encapsulation efficiency (%) = [(total
876 mRNA - free mRNA)/total mRNA] × 100%.
877
878 ***LPP formulated circRNA protection assay***
879 Content analysis was performed to evaluate the integrity of the RNA after the
880 formulation process and to assess RNase protection of the encapsulated RNA.
881 For the RNase protection assay, 1 mAU of RNase A (Thermo Scientific) per
882 microgram of RNA were added to the LPP/LNP/RNA formulation for 30 min at
883 room temperature. RNase was then inactivated by incubating the sample with
884 1.68 mAU/μg RNA of proteinase K (Thermo Scientific) at 55 °C for 10 min.
885 After RNase inactivation, residual RNA was detected from formulations (as
886 described in the *mRNA concentration and encapsulation efficiency of LPP-mRNA*
887 above).
888
889 ***Fluorescent microscopy imaging of circRNA expression***
890 For the experiments where eGFP-mRNA was transfected, 5×10^5 HSkMC cells
891 were incubated with 2 μg of eGFP-mRNA packaged in LPP or lipofectamine
892 (Thermo Scientific) for 24 h in 6-well plate, and eGFP expression was visualized
893 using an Eclipse DMi8 fluorescent microscope (Leica). Frequency of
894 eGFP-expressing cells was determined using flow cytometry (BD FACSCanto II,
895 Becton Dickinson). The excitation and emission was set at 488 nm and 525 nm,
896 respectively.
897
898 ***In vivo biodistribution of FLuc encoded LPP-circRNAs in mice***
899 Female balb/c mice aged 6-8 weeks were purchased from Shanghai Model
900 Organisms Center. 5 μg of LPP formulated circRNA or linear RNA encoding
901 Firefly Luciferase (FLuc) in PBS were administrated into mice (n=3 for each
902 group) intramuscularly with 3/10 insulin syringes (BD biosciences). Mice were
903 then anesthetized for whole-body bioluminescence imaging with an IVIS
904 Spectrum (Roper Scientific) at different time points (6h, 24h, 48h, 72h, 96h and
905 192h).
906
907 ***Administration of LPP circRNA vaccine in mice***
908 For immunogenicity studies, female balb/c mice (Shanghai Model Organisms
909 Center) aged 6-8 weeks old (n=5 for each group) were used. 2 μg of LPP
910 formulated circRNA vaccines were diluted in 50μL 1×PBS buffer and
911 intramuscularly administrated into the mice's same hind leg for both prime and
912 boost shots at an interval of two weeks. Mice in the control groups received PBS.
913 The blood samples were collected on Day 10, 14, 21 & 28 post prime dosing.

914 Mice spleens were also harvested at the endpoint (D28) for ELISpot and flow
915 cytometry.
916
917 ***pVNT measurement***
918 A pseudovirus neutralization assay was performed to evaluate the neutralizing
919 ability of sera collected from immunized mice as described previously[ref]. In
920 brief, serially diluted antibodies were first incubated with pseudotyped virus
921 (Beijing Tiantan Biological) for 1 h, and the mixture was then incubated with
922 BHK-21 cells. After a 24-h incubation in an incubator at 37 °C, cells were
923 collected and lysed with luciferase substrate (PerkinElmer), then underwent
924 luminescence intensity measurement by BioTek microplate reader. The IC50
925 value was calculated using 4 parameter logistic non-linear regression.
926
927 ***Enzyme-Linked ImmunoSorbent Assays (ELISA)***
928 Briefly, recombinant VZV gE protein (Genscript) diluted in coating buffer
929 (Biolegend) were used to coat 96-well EIA/RIA plates (Greiner Bio-one, 100
930 ng/well) at 4°C overnight. The plates were then washed with 1× PBS-T (0.05%
931 Tween-20) and blocked with 2% BSA in PBS-T for 2 hours at RT. Mice sera
932 samples with serial dilutions were added and incubated for 2 hours at RT. After
933 washing, HRP-conjugated goat anti-mouse IgG Ab (1:10,000) was added and
934 incubated for 1 hour. TMB substrate (Invitrogen) was then used for color
935 development and the absorbance was read at 450 nm using BioTek microplate
936 reader. Endpoint titers were calculated as the largest sample dilution factor
937 yielding a signal that exceeds 2.1-fold value of the background.
938
939 ***In vivo mouse cytokine analysis***
940 A serial dosage of LPP formulated CR3, CR-Novo and LR-Novo (0.02 μg, 0.2 μg,
941 2 μg) were intramuscularly administered into female Balb/c mice (n=5, Shanghai
942 Model Organisms Center) aged 6-8 weeks old. Mice sera were collected
943 retro-orbitally at 4 h and 7 days post administration and subjected to cytokine
944 analysis (Cytometric Bead Array Mouse Inflammation Kit, BD) using flow
945 cytometry following the manufacturer's instructions. Data were presented as the
946 percentage change relative to baseline mice group administered with PBS.
947
948 ***IFN-γ ELISpots***
949 Assessment of the IFN-γ T cell response was performed using the Mouse IFN-γ
950 ELISpotPLUS kit (Mabtech) following the manufacturer's instructions. Briefly,
951 anti-IFN-γ pre-coated plates were blocked with DMEM+10% FBS for at least 30
952 min, then cells were added at 3×10^5 cells per well for negative control (media
953 only) and RABV-G or VZV-gE peptide pools (15-mers overlapping by 11;
954 Genscript) (1 μg/mL) in 200 μL final volume per well. The positive control wells
955 contained 5×10^4 cells per well in 200 μL final volume per well with 5 μg/mL of

956 ConA. Plates were incubated overnight at 5% CO_2, 37 °C incubator and
957 developed as per the manufacturer's protocol. After overnight stimulation, plates
958 were washed and sequentially incubated with biotinylated IFN-γ detection
959 antibody (R4-6A2), streptavidin-ALP, and finally BCIP/NBT. Plates were
960 imaged with ImmunoSpot Analyzer and quantified with ImmunoSpot software.
961
962 ***Biodistribution of LPP-circRNA***
963 The mice were divided into two groups, and 5 μg CR-Novo-LPP or CR3-LPP was
964 injected into the hind legs, respectively. 5 mices in each group were euthanized at
965 2h, 6h, 24h, 48h, 72h and 168h after administration. Tissue samples including
966 heart, liver, spleen, lung, kidney, small intestine, brain, muscle at the injection site,
967 and lymph node were collected and rapidly frozen in liquid nitrogen, and RNA
968 was extracted using trizol method. The levels of CR-Novo or CR3 in tissue
969 samples were analyzed by RT-qPCR. GraphPad Prism 8 and Origin2021 software
970 were used for data processing.
971 Gene specific TaqMan primers amplifying the circRNA junction site were
972 synthesized (TsingKe) as below:
973 circ-tzF (5'-3'): ACAAACGGCTATTATGCGTTACC;
974 circ-tzR (5'-3'): GACTTGAACCCACACGACCG;
975 circ-Probe (5'-3'): FAM-ACGGACTTAAAATCCGTTGAC-MGB
976 Target amplification sequence was inserted into plasmid as an internal standard to
977 obtain the absolute circRNA copies from RNA extracts. The qPCR reaction was
978 carried out using Probe qPCR Mix kit (Takara). For each sample, threshold cycle
979 values (Ct) were processed according to the comparative Ct method. Gene
980 expression levels were presented relative to Standard curve.
981
982 ***Correlation analysis***
983 The Pearson correlation coefficient was calculated to assess the relationship
984 between continuous variables, for example, experiment half-life and MFE.
985
986 ***Statistical Analyses***
987 Two-tailed Student t test was used to determine statistical significance for data
988 comparisons at a single time point. One-way ANOVA was used to determine
989 statistical significance for data comparisons with multiple time points. Prism
990 version 8.0 (GraphPad) or Origin 10.0 were used for generation of all graphs and
991 performance of statistical analyses. Statistical significance is denoted as ns, not
992 significant, *$p < 0.05$, **$p < 0.01$, and ***$p < 0.001$.
993

994 # Data Availability

995 The RNA sequences and DNA primer sequences used in the biological
996 experiments are included in the Supplementary Sequence Information section (at
997 the end of the manuscript). and are also uploaded in the submission system. We
998 will release data at a permanent location upon acceptance and the accession codes

will be available before publication.

Code Availability

The code has been submitted as part of this submission and will be released at a permanent location upon acceptance.

Conflict of Interest

L.H. is the founder of Coderna.ai. C.X., W.W., Y.T., H.S., Y.Y., Q.W., H.S., and H.L. are employees of StemiRNA Therapeutics. C.X., W.W., Y.T., H.S., and H.L. have filed provisional patents for the circRNA rabies and VZV vaccines.

Author Contributions

H.L. conceived and directed the project. H.L., H.S. and C.X. supervised all the *in vitro* and *in vivo* experiments. L.Z. and L.H. developed the circDesign algorithm to design circRNA sequences. C.X., W.W., X.W. and J.A. performed the mRNA synthesis and gel electrophoresis experiments. H.X., X.Q. and M.S. performed the liquid chromatography analysis and purification. C.X., W.W., J.A., X.S., Y.Y. and H.S. performed the protein expression and *in vivo* assays, and Q.W. conducted LPP formulation and chemical stability assays. Y.T. performed the ribo-seq experiments. H.Z. and Y.G. performed the animal study including injection and *in vivo* imaging. C.X., L.Z., H.L., H.S., W.W., Y.T., Q.W., and L.H. wrote the manuscript.

Acknowledgements

We thank the assistance from colleagues including Xinxin Su, Mingyang Liu, and Kun Xie at StemiRNA Therapeutics in animal experiments. Congcong Xu is sponsored by Shanghai Pujiang Talent Program (22PJ1423100). The funds from StemiRNA Therapeutics were supported by the Science and Technology Commission of Shanghai Municipality, China (20S11909100, 22S11902300; Shanghai Strategic Emerging Industry Development special fund (ZJ640070216) and the project of mRNA Innovation and Translation Center, Shanghai, China.

Figure Legends

Figure 1. circDesign approach overview and design of circular RNA molecules encoding RABV-G. a, circDesign workflow illustration from library screening to structure-based analysis. Given a specific amino acid sequence, mRNA sequence pool was generated followed by candidate screening based on MFE and CAI. By incorporation of ORF into circRNA backbone, the circRNA folding, ensemble

1037 diversity and cross-region interaction was assessed. The designed circRNAs were
1038 then evaluated in vitro and in vivo. b, Distribution of circDesign-generated ORFs
1039 (R1-R6) and benchmark sequences (Ther & Novo) in a two-dimensional plot. The
1040 color darkness indicates the ensemble diversity. Schematic illustration of
1041 circRNA sequence designs composed of different functional regions for
1042 circularization. Homo arm refers to homology arm for 5'- & 3'- end pairing. c,
1043 Representative circularized diagram showing the CR3 and CR-Novo sequence. d,
1044 Secondary structure of CR3 and CR-Novo (uncolored: IRES motif; red: loop
1045 structure; blue: stem structure). e, Pairwise visualization of CR3 and CR-Novo
1046 showing the intra- and inter-region interaction (red: inter-region interaction; blue:
1047 inter-region interaction). Each region was colored as indicated.

1048 **Figure 2.** Characterization of circular RNA molecules encoding RABV-G. a,
1049 Comparison of the circularization efficiency of different circRNA using qPCR
1050 method. Data in triplicate were presented as mean ± s.d. b, Native agarose gel
1051 characterization of the circRNA showing the correlation of gel mobility with
1052 circRNA folding compactness. c, Thermodynamic stability of circRNA
1053 molecules suggesting a correlation of MFE with melting temperature. The mean
1054 values of three independent measurement data were fitted with sigmoidal curve to
1055 extrapolate the melting temperature. d, In-solution degradation curve of circRNA
1056 upon incubation in PBS buffer containing 10 mM Mg^{2+} at 37 °C. Triplicate data
1057 were presented as mean ± s.d. and fitted with one-phase decay curve to obtain
1058 half-life and decay constant. e, In-cell degradation of all circRNAs within 72 h
1059 post-transfection in HSkMC cells. Triplicate data points were presented as mean
1060 ± s.d. followed by non-linear one-phase decay fitting. The original value at the 0 h
1061 was set as 125% with a final plateau value at 0%. f, Flow cytometry analysis of
1062 circRNA in comparison with linear RNA in HSkMC cells at 24 h
1063 post-transfection. Mean fluorescent intensity (MFI) of protein expression level
1064 from cells transfected circRNA or linear mRNA was calculated. Three
1065 independent measurement data were plotted as mean ± s.d. One-way ANOVA
1066 with multiple comparisons to LR-Novo group was performed for statistical
1067 analysis. g, Correlation analysis of MFE with experiment in-solution and in-cell
1068 half-life. h, Correlation analysis of predicted half-life with experiment half-life.

1069 **Figure 3.** Translation efficiency comparison of CR3 and CR-Novo. Predicted
1070 secondary structure of a) CR3 and b) CR-Novo. c, Simplified workflow diagram
1071 of ribosome profiling and polysome profiling of circRNA. d, Abundance of
1072 Ribo-seq and RNA-seq counts of circRNA (CR3 & CR-Novo) in transfected cells
1073 showing the higher translation efficiency of CR3. d, Total RNA-seq and Ribo-seq

1074 fpkm of CR-Novo and CR3 showing the relatively higher RNA abundance and
1075 higher ribosome footprint counts in cellular context. e, circular barplot showing
1076 the ribosome footprints of CR3 and CR-Novo. h, Polysome profiling results of
1077 CR3 and CR-Novo. f, Total polysome profiling of CR3 (black) and CR-Novo (red)
1078 transfected cells. g, RT-qPCR quantification of CR3 (black) and CR-Novo in
1079 collected ultracentrifuge fractions. The colored region refers to different major
1080 fractions from 40S, 60S, 80S (monosome) to polysomes. Data in triplicate
1081 measurement were presented as mean ± s.e.m.

1082 **Figure 4.** Characterization of LPP formulated circRNAs. a, Scheme of two-step
1083 manufacturing of LPP formulated circRNA. The lipid mixture contains ionizable
1084 lipid, PEGylated lipid, cholesterol and helper lipid. b, The hydrodynamic size and
1085 polydispersity index (PDI) of LPP formulated linear RNA (LR-Fluc) and circular
1086 RNA (CR-FLuc). Zeta potential of LPP formulated circRNA and linear RNA.
1087 Three independent measurement data were plotted as mean ± s.e.m. d,
1088 Representative whole-body IVIS images of mice administered LPP CR-FLuc or
1089 LR-FLuc at different time points (6h, 24h, 48h, 72h, 96h and 168h). e. Total flux
1090 curve of luminescence as a function of time in balb/c mice (n=3; Green:
1091 CR-FLuc-LPP; Pink: LR-FLuc-LPP; Grey: PBS). f, Area under the curve (AUC)
1092 calculation of three groups from 6 h to 168 h suggesting the accumulated
1093 luciferase activity over the time course. Each dot represented the mean ± s.e.m. of
1094 data from three mice. Statistical significance was determined by One-way
1095 ANOVA multiple comparisons with LR-FLuc, ***$p < 0.001$; **$p < 0.01$; *$p <$
1096 0.05; ns, not significant. g, Hydrodynamic size and PDI of LPP formulated
1097 circRNA and linear RNA. Three independent measurement data were plotted as
1098 mean ± s.e.m. h, Zeta potential of LPP formulated circRNA and linear RNA.
1099 Three independent measurement data were plotted as mean ± s.e.m. i, Storage
1100 stability of LPP formulated circRNA and linear RNA at 4°C implying the shelf
1101 life of circRNA vaccines. Samples in triplicate were treated and tested. The data
1102 to each sample were normalized to its D0 as 1 and plotted as mean ± s.e.m.

1103 **Figure 5**. In vivo immune responses induced by circRNA rabies vaccine. a,
1104 Balb/c mice (n=5) immunization schedule and proposed mechanism of action of
1105 LPP circRNA rabies vaccines. Pseudovirus neutralizing titer (pVNT) of mice sera
1106 immunized with two doses of LPP formulated RNA vaccines on b) D10, c) D14, d)
1107 D21 and e) D28. pVNT data were presented as geometric mean ± geometric s.d. f,
1108 The geometric increase (GMI) of pVNT from mice vaccinated with different
1109 RNA vaccines using D10 pVNT as the baseline. GMI data were plotted with
1110 geometric s.d. g, IFN-γ ELISpot analysis of mice splenocytes on Day 28 showing

robust cellular immune responses triggered by circDesign optimized sequences. Data in graph represented as s.f.c. per 3*10^5 cells. Each point on violin plot represents a single mouse. Bold black line represents the median. The significance between groups was determined using a one-way ANOVA with Dunn's multiple comparison test, ***p < 0.001; **p < 0.01; *p < 0.05; ns, not significant. s.f.c., spot-forming cells. h, Summary of pVNT results from D10 to D28 of all vaccinated balb/c mice (n=5) Data were presented as geometric mean ± geometric s.d.

Figure 6. In vivo biodistribution and immune response longevity analysis of LPP formulated rabies vaccines. In vivo biodistribution of LPP formulated circRNA. RT-qPCR quantification of a) CR-Novo and b) CR3 in different tissues at different time points (6h, 24h, 48h, 72h and 168h) in balb/c mice (n=5 per group at each time point). c, Pie plot showing the tissue distribution of circular RNA at various time points. d, Parallel comparison of circRNA abundance in muscle tissue as a function of time. Statistical significance was determined by multiple Mann-Whitney u tests ***p < 0.001; **p < 0.01; *p < 0.05; ns, not significant. e, Scheme of immunization schedule in balb/c mice study (n=5). f, Pseudovirus neutralizing antibody titer kinetics of CR3 and CR-Novo. Data were presented as geometric mean ± geometric s.d. Statistical significance was determined by multiple Mann-Whitney u tests ***p < 0.001; **p < 0.01; *p < 0.05; ns, not significant. g, IFN-γ and TNF-α ELISpot analysis of mice splenocytes on Day 28 showing robust cellular immune responses triggered by CR3. Data in graph represented as s.f.c. per 3*10^5 cells. Each point on violin plot represents a single mouse. Bold black line represents the median. The significance between groups was determined using a one-way ANOVA with Dunn's multiple comparison test, ***p < 0.001; **p < 0.01; *p < 0.05; ns, not significant. s.f.c., spot-forming cells.

Figure 1

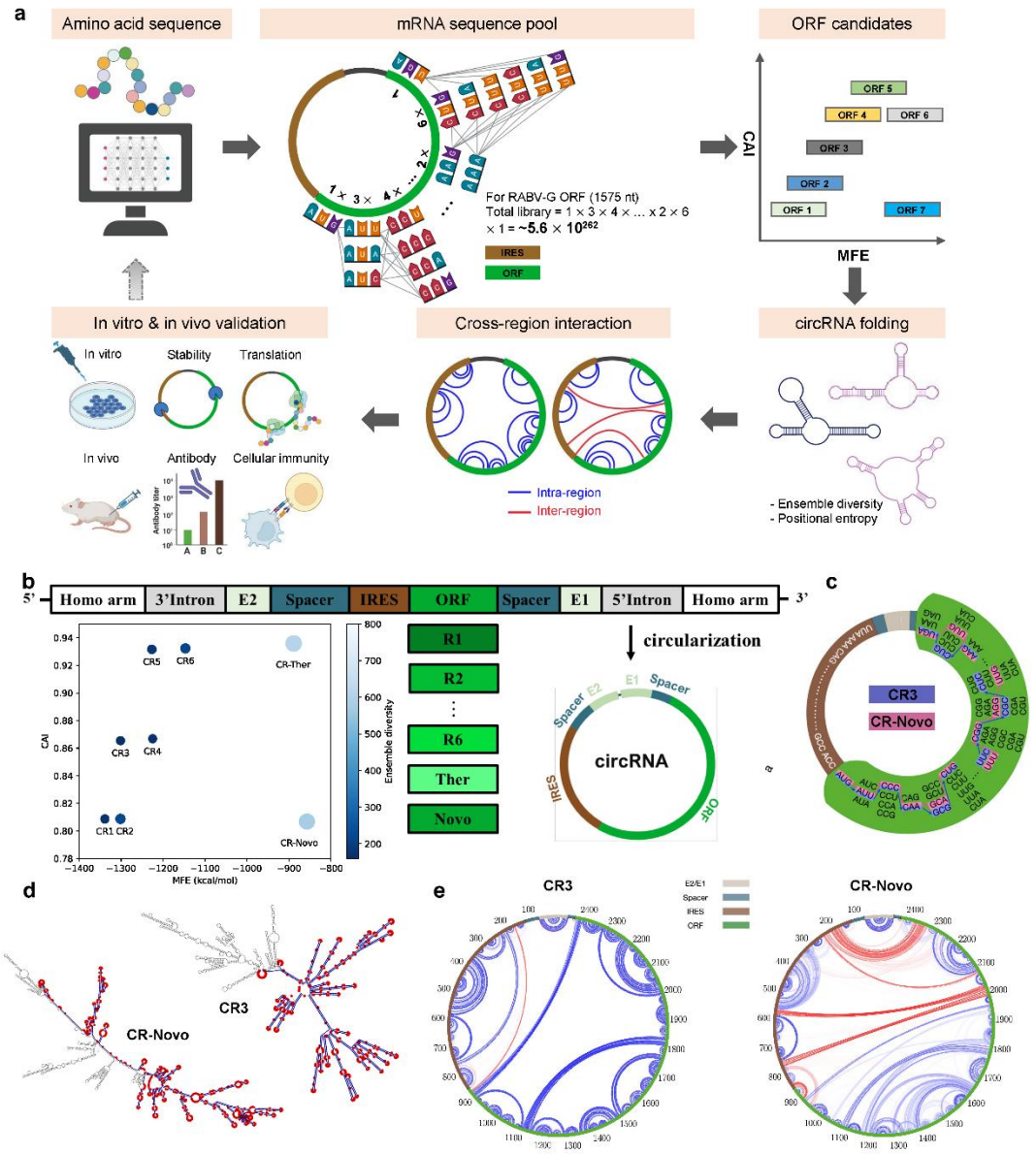

1142

Figure 2

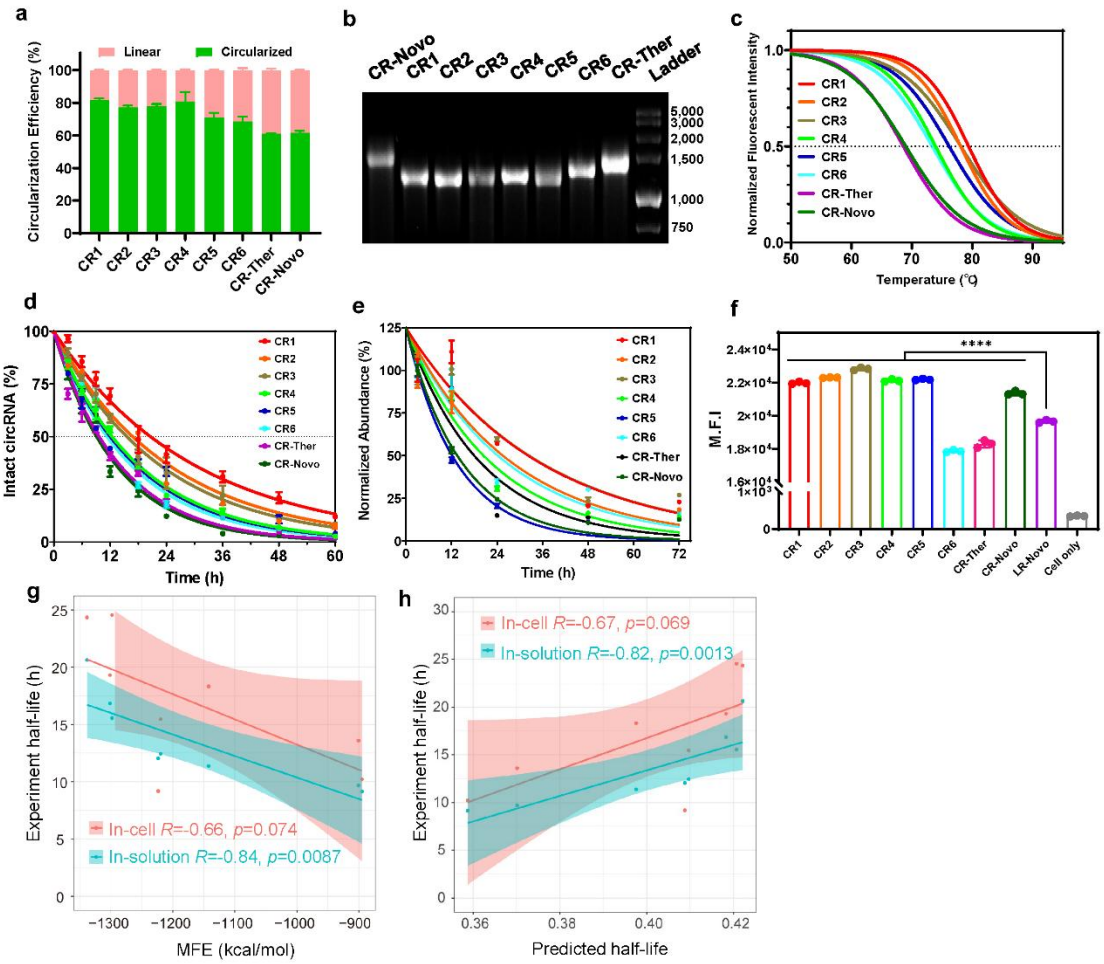

1143

Figure 3

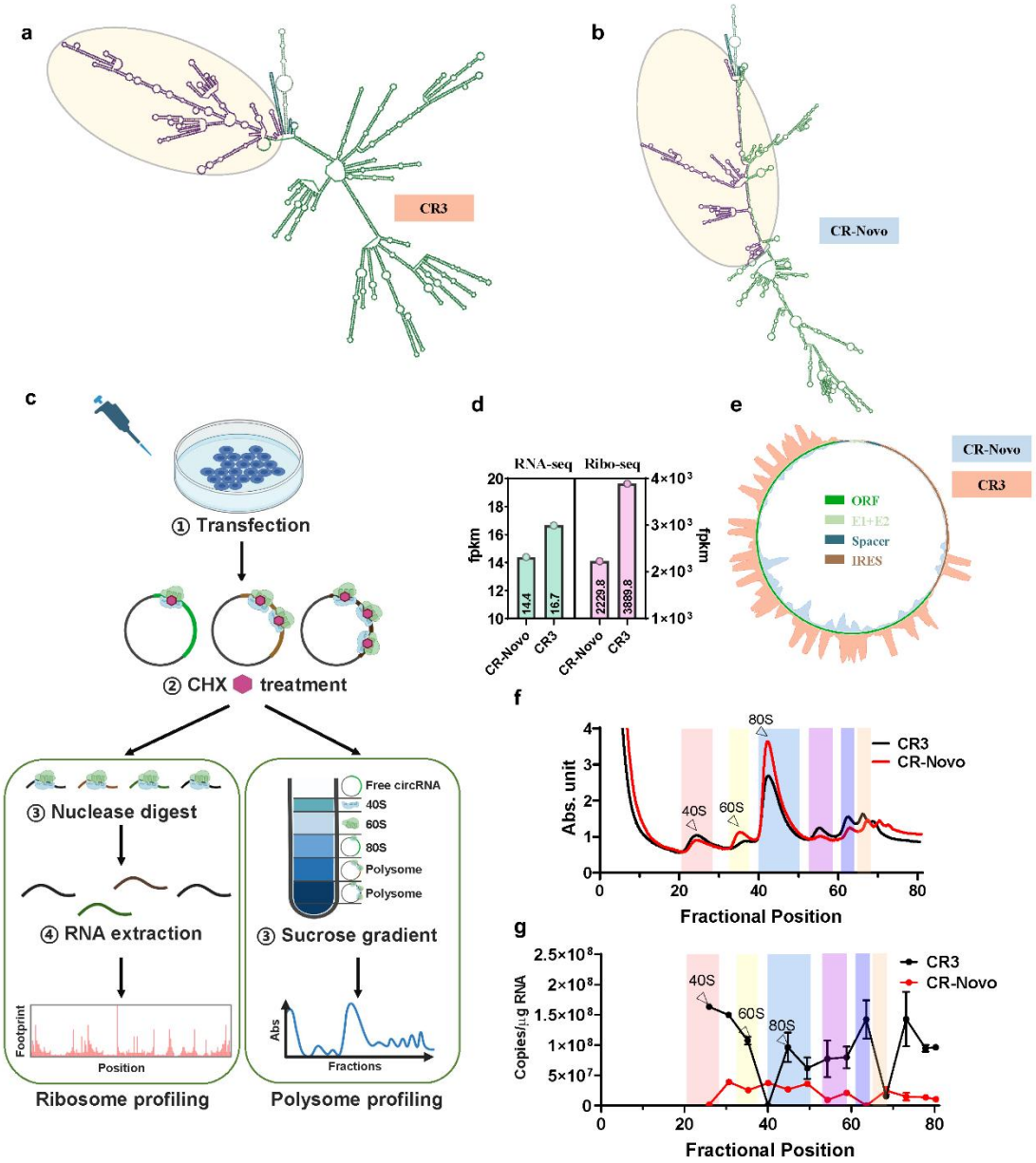

1144

Figure 4

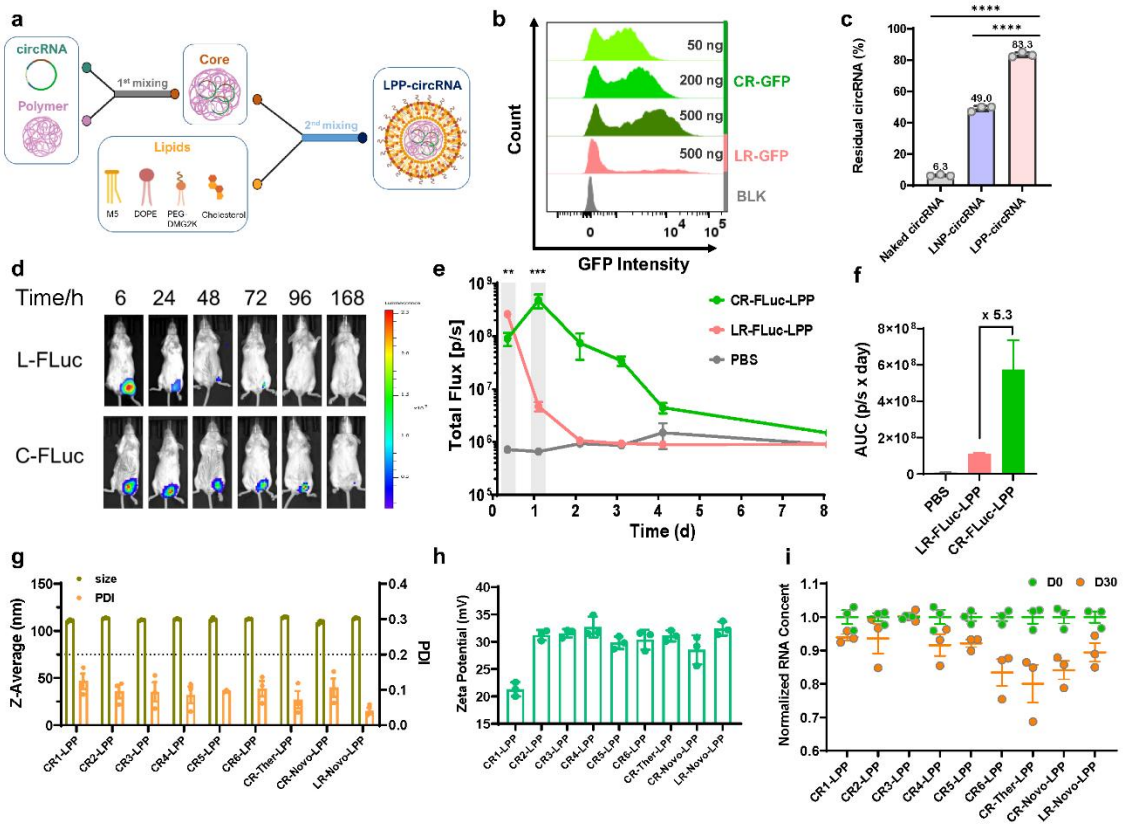

1145

Figure 5

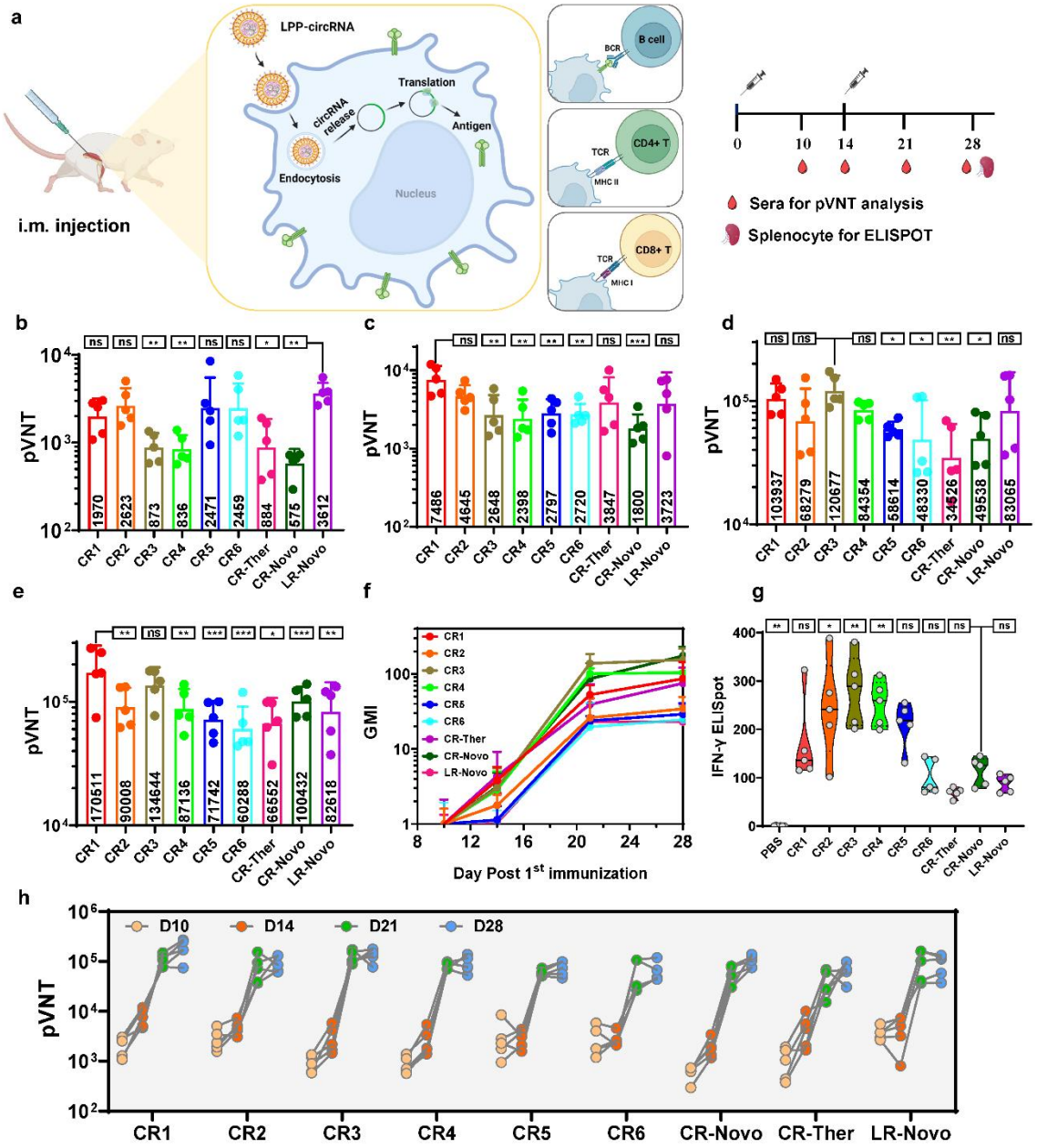

1146

Figure 6

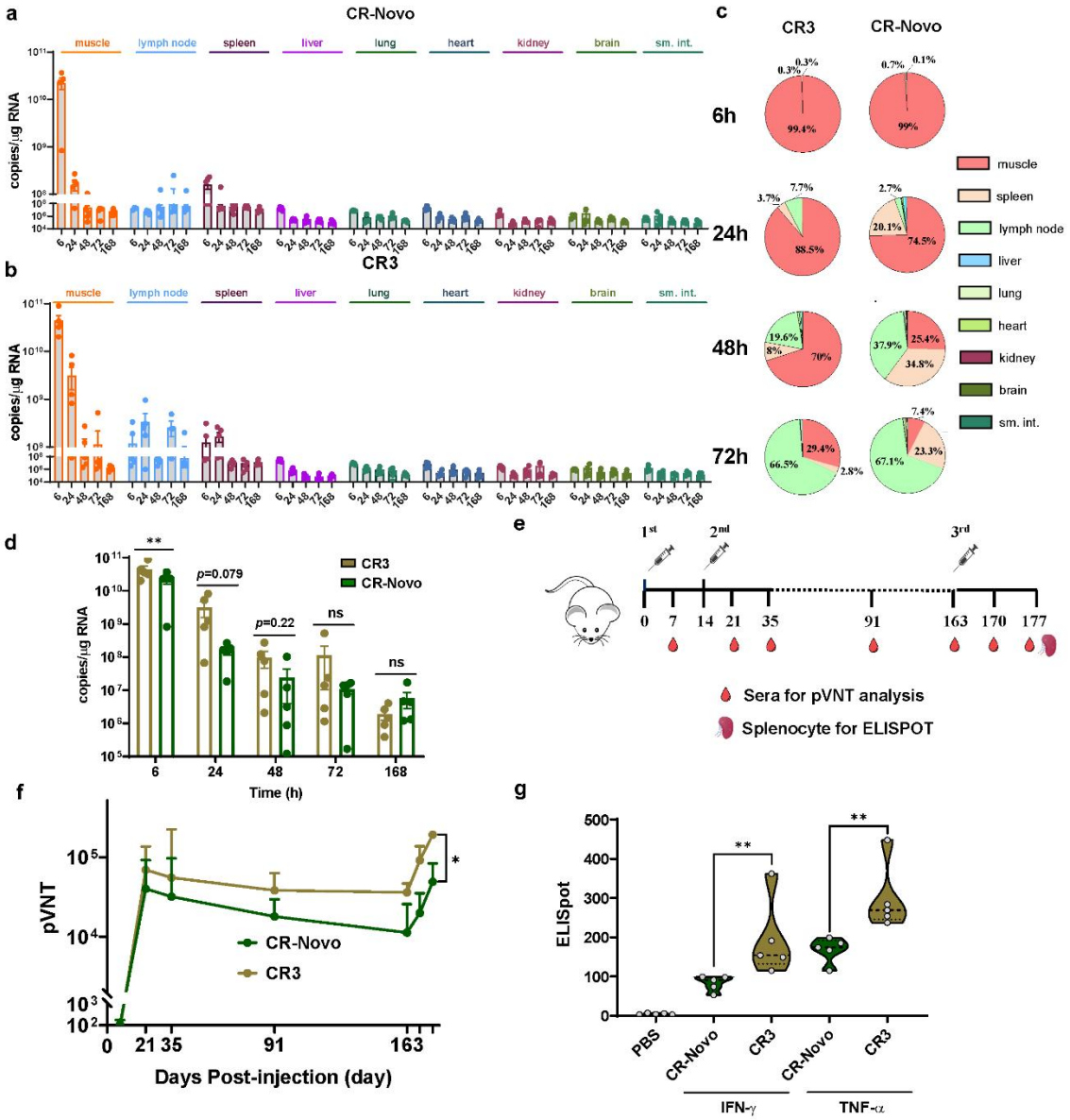

1147

1148

1149 # References

1150 1. Leppek, K. et al. Combinatorial optimization of mRNA structure, stability,
1151 and translation for RNA-based therapeutics. *Nat Commun* **13**, 1536 (2022).
1152 2. Trepotec, Z. et al. Maximizing the Translational Yield of mRNA
1153 Therapeutics by Minimizing 5'-UTRs. *Tissue Eng Part A* **25**, 69-79 (2019).
1154 3. Orlandini von Niessen, A.G. et al. Improving mRNA-Based Therapeutic
1155 Gene Delivery by Expression-Augmenting 3' UTRs Identified by Cellular
1156 Library Screening. *Mol Ther* **27**, 824-836 (2019).
1157 4. Xia, X. Detailed Dissection and Critical Evaluation of the Pfizer/BioNTech
1158 and Moderna mRNA Vaccines. *Vaccines (Basel)* **9** (2021).
1159 5. Mauger, D.M. et al. mRNA structure regulates protein expression through
1160 changes in functional half-life. *Proc Natl Acad Sci U S A* **116**, 24075-24083
1161 (2019).
1162 6. Zhang, H. et al. Algorithm for Optimized mRNA Design Improves
1163 Stability and Immunogenicity. *Nature* (2023).
1164 7. Meganck, R.M. et al. Engineering highly efficient backsplicing and
1165 translation of synthetic circRNAs. *Mol Ther Nucleic Acids* **23**, 821-834
1166 (2021).
1167 8. Katrekar, D. et al. Efficient in vitro and in vivo RNA editing via
1168 recruitment of endogenous ADARs using circular guide RNAs. *Nat*
1169 *Biotechnol* **40**, 938-945 (2022).
1170 9. Qu, L. et al. Circular RNA Vaccines against SARS-CoV-2 and Emerging
1171 Variants. *Cell* (2022).
1172 10. Wen, S.Y., Qadir, J. & Yang, B.B. Circular RNA translation: novel protein
1173 isoforms and clinical significance. *Trends Mol Med* **28**, 405-420 (2022).
1174 11. Chen, C.K. et al. Structured elements drive extensive circular RNA
1175 translation. *Mol Cell* **81**, 4300-4318 e4313 (2021).
1176 12. Chen, R. et al. Engineering circular RNA for enhanced protein production.
1177 *Nat Biotechnol* **41**, 262-272 (2023).
1178 13. Hofacker, I.L. RNA secondary structure analysis using the Vienna RNA
1179 package. *Curr Protoc Bioinformatics* **Chapter 12**, Unit 12 12 (2004).
1180 14. Garcia-Martin, J.A. & Clote, P. RNA Thermodynamic Structural Entropy.
1181 *PLoS One* **10**, e0137859 (2015).
1182 15. Xia, X. An improved implementation of codon adaptation index. *Evol*
1183 *Bioinform Online* **3**, 53-58 (2007).
1184 16. Schnee, M. et al. An mRNA Vaccine Encoding Rabies Virus Glycoprotein
1185 Induces Protection against Lethal Infection in Mice and Correlates of
1186 Protection in Adult and Newborn Pigs. *PLoS Negl Trop Dis* **10**, e0004746
1187 (2016).
1188 17. Hellgren, F. et al. Unmodified rabies mRNA vaccine elicits high

1189 cross-neutralizing antibody titers and diverse B cell memory responses.
1190 *Nat Commun* **14**, 3713 (2023).
1191 18. Yang, J. et al. Intratumoral delivered novel circular mRNA encoding
1192 cytokines for immune modulation and cancer therapy. *Mol Ther Nucleic*
1193 *Acids* **30**, 184-197 (2022).
1194 19. Amaya, L. et al. Circular RNA vaccine induces potent T cell responses.
1195 *Proc Natl Acad Sci U S A* **120**, e2302191120 (2023).
1196 20. Wesselhoeft, R.A., Kowalski, P.S. & Anderson, D.G. Engineering circular
1197 RNA for potent and stable translation in eukaryotic cells. *Nat Commun* **9**,
1198 2629 (2018).
1199 21. Hofacker, I.L. Energy-directed RNA structure prediction. *Methods Mol*
1200 *Biol* **1097**, 71-84 (2014).
1201 22. Mathews, D.H. Revolutions in RNA secondary structure prediction. *J Mol*
1202 *Biol* **359**, 526-532 (2006).
1203 23. Souii, A., Ben M'hadheb-Gharbi, M. & Gharbi, J. Role of RNA structure
1204 motifs in IRES-dependent translation initiation of the coxsackievirus B3:
1205 new insights for developing live-attenuated strains for vaccines and gene
1206 therapy. *Mol Biotechnol* **55**, 179-202 (2013).
1207 24. Bhattacharyya, S., Verma, B., Pandey, G. & Das, S. The structure and
1208 function of a cis-acting element located upstream of the IRES that
1209 influences Coxsackievirus B3 RNA translation. *Virology* **377**, 345-354
1210 (2008).
1211 25. Packer, M., Gyawali, D., Yerabolu, R., Schariter, J. & White, P. A novel
1212 mechanism for the loss of mRNA activity in lipid nanoparticle delivery
1213 systems. *Nat Commun* **12**, 6777 (2021).
1214 26. Crommelin, D.J.A., Anchordoquy, T.J., Volkin, D.B., Jiskoot, W. &
1215 Mastrobattista, E. Addressing the Cold Reality of mRNA Vaccine Stability.
1216 *J Pharm Sci* **110**, 997-1001 (2021).
1217 27. Jeck, W.R. & Sharpless, N.E. Detecting and characterizing circular RNAs.
1218 *Nat Biotechnol* **32**, 453-461 (2014).
1219 28. Garneau, N.L., Wilusz, J. & Wilusz, C.J. The highways and byways of
1220 mRNA decay. *Nat Rev Mol Cell Biol* **8**, 113-126 (2007).
1221 29. Guo, Y., Wei, X. & Peng, Y. Structure-Mediated Degradation of
1222 CircRNAs. *Trends Cell Biol* **30**, 501-503 (2020).
1223 30. Labno, A., Tomecki, R. & Dziembowski, A. Cytoplasmic RNA decay
1224 pathways - Enzymes and mechanisms. *Biochim Biophys Acta* **1863**,
1225 3125-3147 (2016).
1226 31. Chen, L.L. The expanding regulatory mechanisms and cellular functions of
1227 circular RNAs. *Nat Rev Mol Cell Biol* **21**, 475-490 (2020).
1228 32. Ingolia, N.T., Brar, G.A., Rouskin, S., McGeachy, A.M. & Weissman, J.S.
1229 The ribosome profiling strategy for monitoring translation in vivo by deep

1230 sequencing of ribosome-protected mRNA fragments. *Nat Protoc* **7**,
1231 1534-1550 (2012).
1232 33. Pringle, E.S., McCormick, C. & Cheng, Z. Polysome Profiling Analysis of
1233 mRNA and Associated Proteins Engaged in Translation. *Curr Protoc Mol*
1234 *Biol* **125**, e79 (2019).
1235 34. Brar, G.A. & Weissman, J.S. Ribosome profiling reveals the what, when,
1236 where and how of protein synthesis. *Nat Rev Mol Cell Biol* **16**, 651-664
1237 (2015).
1238 35. Yang, R. et al. A core-shell structured COVID-19 mRNA vaccine with
1239 favorable biodistribution pattern and promising immunity. *Signal*
1240 *Transduct Target Ther* **6**, 213 (2021).
1241 36. Meng, C. et al. Virus-Mimic mRNA Vaccine for Cancer Treatment. *Adv*
1242 *Ther (Weinh)* **4**, 2100144 (2021).
1243 37. Tan, Y. et al. Single-cell transcriptome atlas reveals protective
1244 characteristics of COVID-19 mRNA vaccine. *J Med Virol* **95**, e28161
1245 (2023).
1246 38. Gui, Y.Z. et al. Safety and immunogenicity of a modified COVID-19
1247 mRNA vaccine, SW-BIC-213, as a heterologous booster in healthy adults:
1248 an open-labeled, two-centered and multi-arm randomised, phase 1 trial.
1249 *EBioMedicine* **91**, 104586 (2023).
1250 39. Johnson, N., Cunningham, A.F. & Fooks, A.R. The immune response to
1251 rabies virus infection and vaccination. *Vaccine* **28**, 3896-3901 (2010).
1252 40. Venkataswamy, M.M. et al. Cellular immune response following
1253 pre-exposure and postexposure rabies vaccination by intradermal and
1254 intramuscular routes. *Clin Exp Vaccine Res* **4**, 68-74 (2015).
1255 41. Overduin, L.A., van Dongen, J.J.M. & Visser, L.G. The Cellular Immune
1256 Response to Rabies Vaccination: A Systematic Review. *Vaccines (Basel)* **7**
1257 (2019).
1258 42. Mills, D.J., Lau, C.L., Mills, C. & Furuya-Kanamori, L. Long-term
1259 persistence of antibodies and boostability after rabies intradermal
1260 pre-exposure prophylaxis. *J Travel Med* **29** (2022).
1261 43. Arvin, A.M. Humoral and cellular immunity to varicella-zoster virus: an
1262 overview. *J Infect Dis* **197 Suppl 2**, S58-60 (2008).
1263 44. Zhang, L. et al. The role of N(6)-methyladenosine (m(6)A) modification in
1264 the regulation of circRNAs. *Mol Cancer* **19**, 105 (2020).
1265 45. Meyer, K.D. et al. 5' UTR m(6)A Promotes Cap-Independent Translation.
1266 *Cell* **163**, 999-1010 (2015).
1267 46. Lorenz, R. et al. ViennaRNA Package 2.0. *Algorithms Mol Biol* **6**, 26
1268 (2011).
1269

Extended Data Figure 1

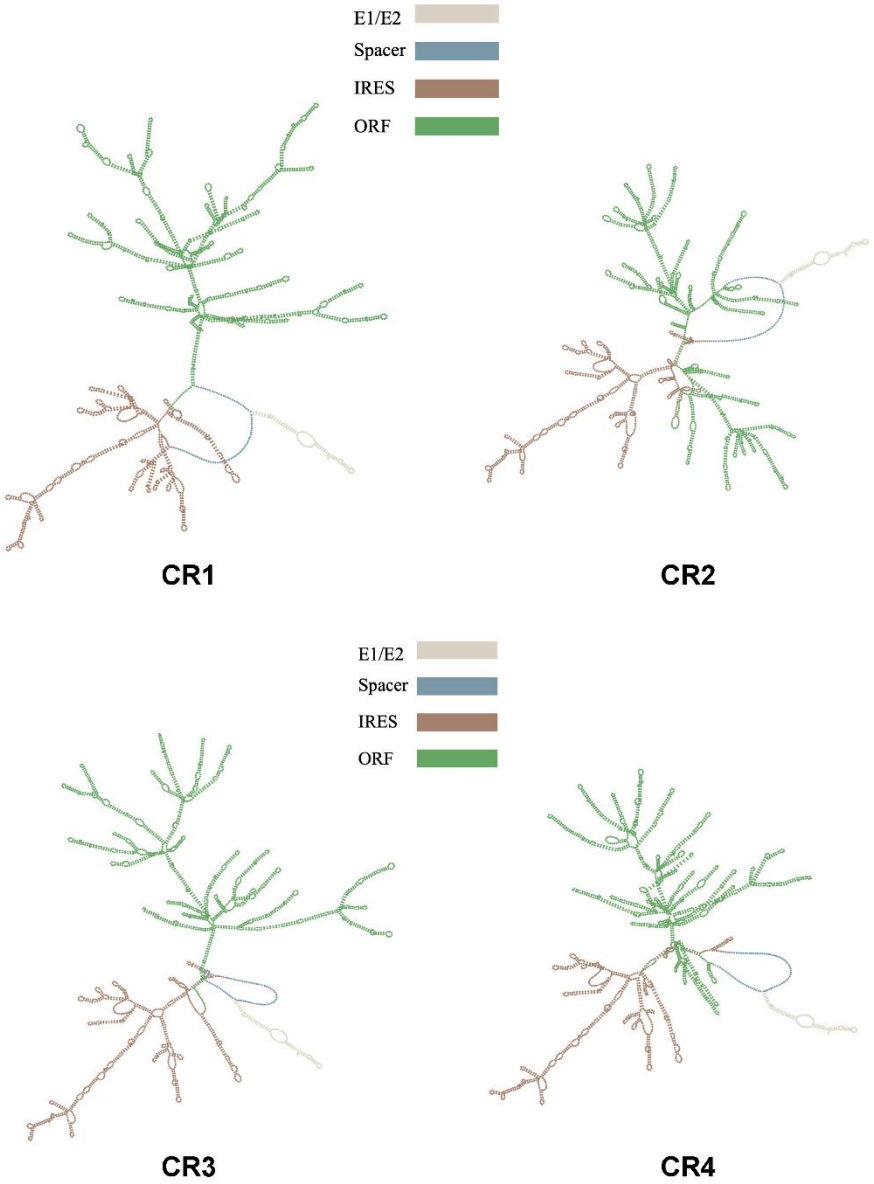

Extended Data Figure 2

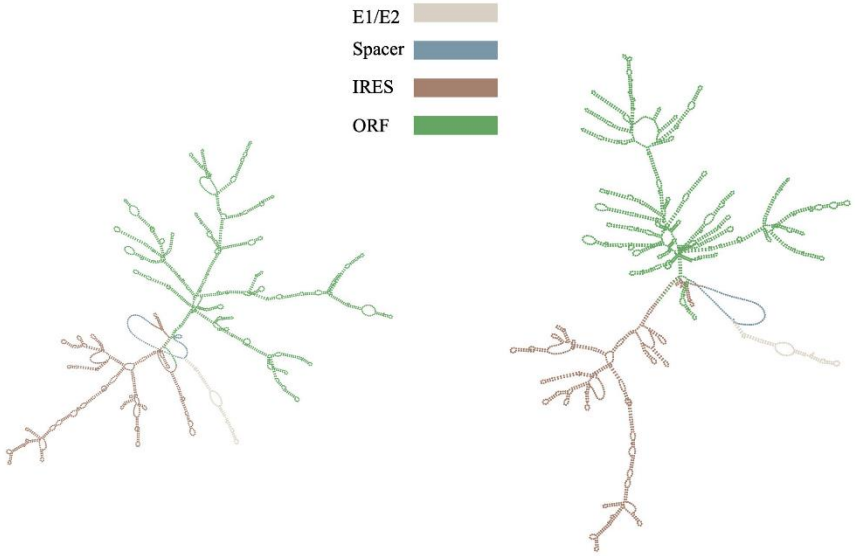

CR5 **CR6**

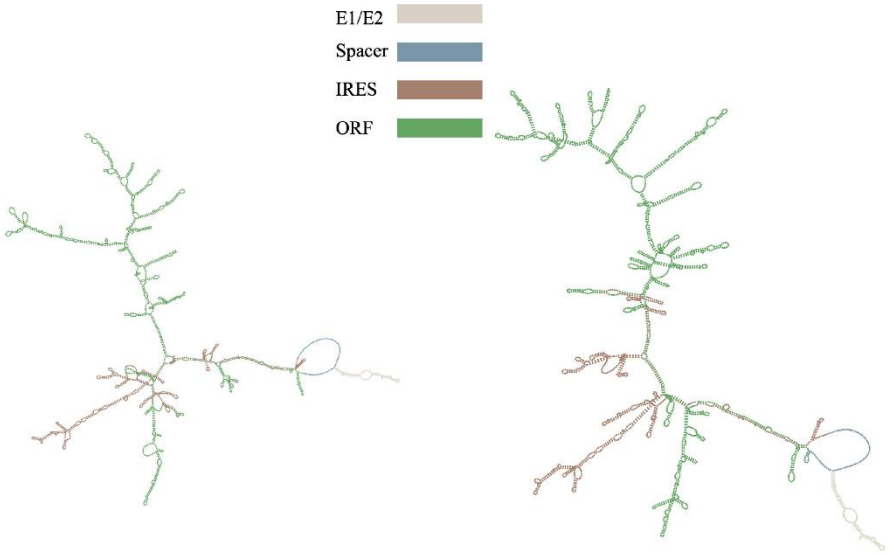

CR-Ther **CR-Novo**

Extended Data Figure 3

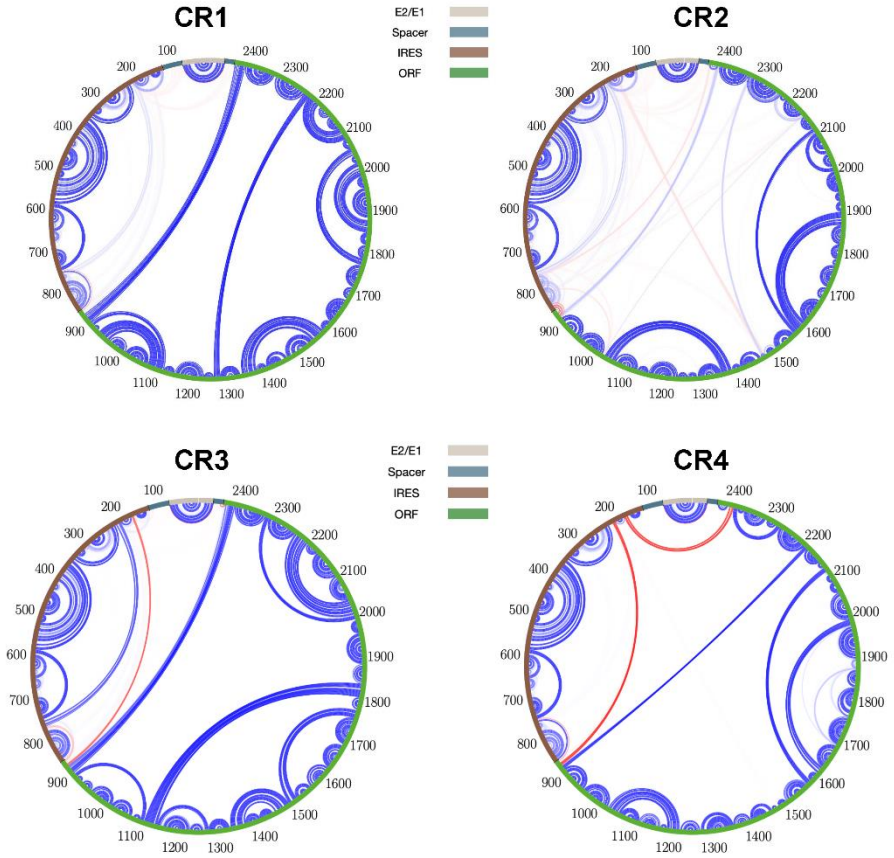

Extended Data Figure 4

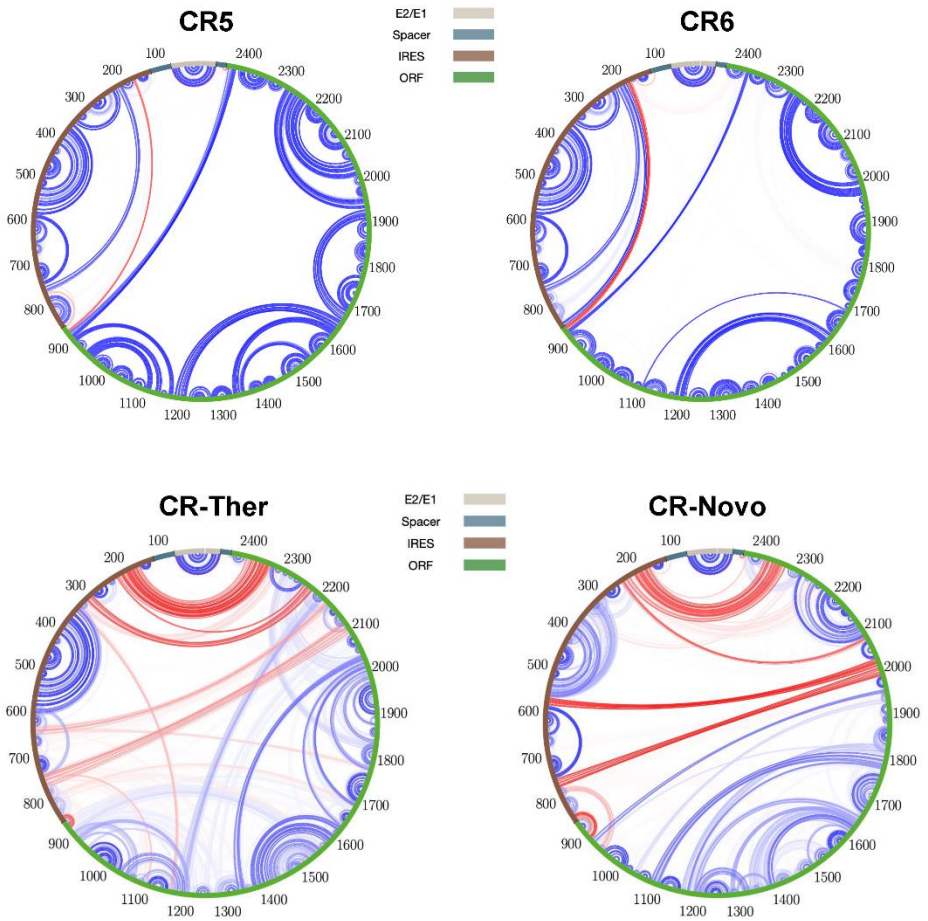

Extended Data Figure 5

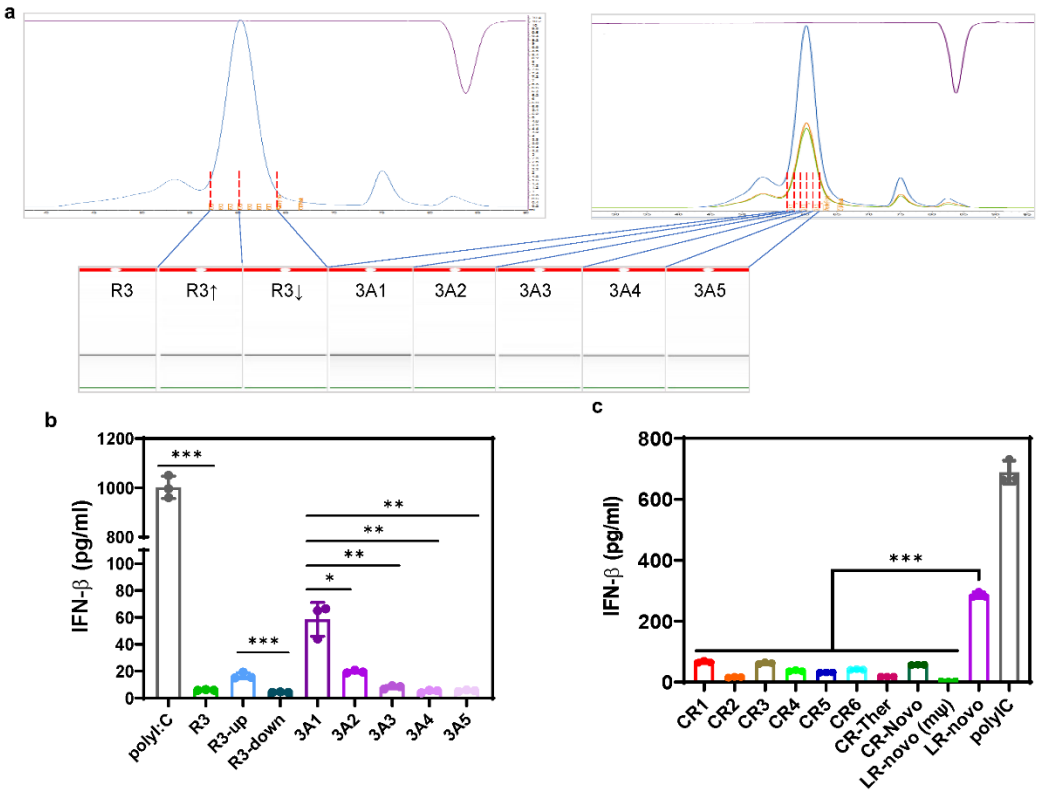

Extended Data Figure 6

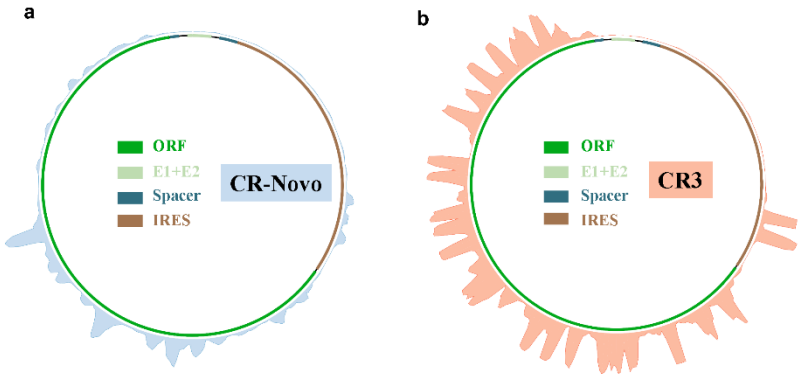

Extended Data Figure 7

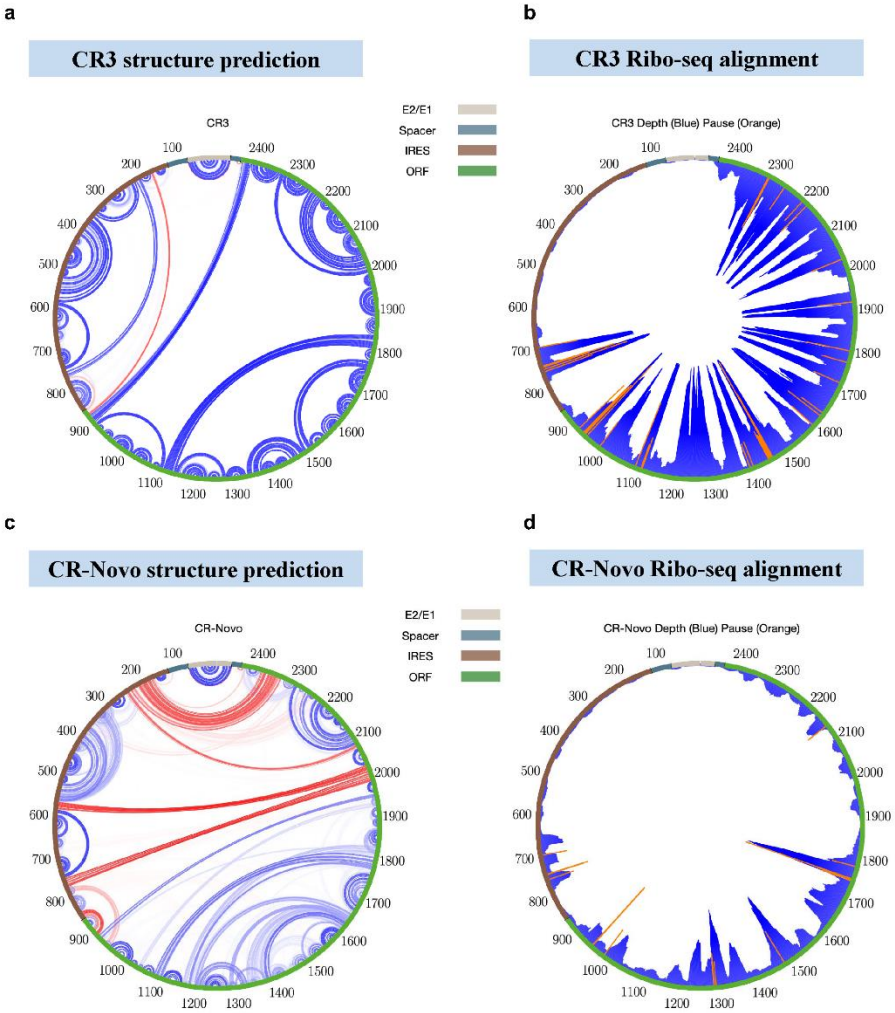

Extended Data Figure 8

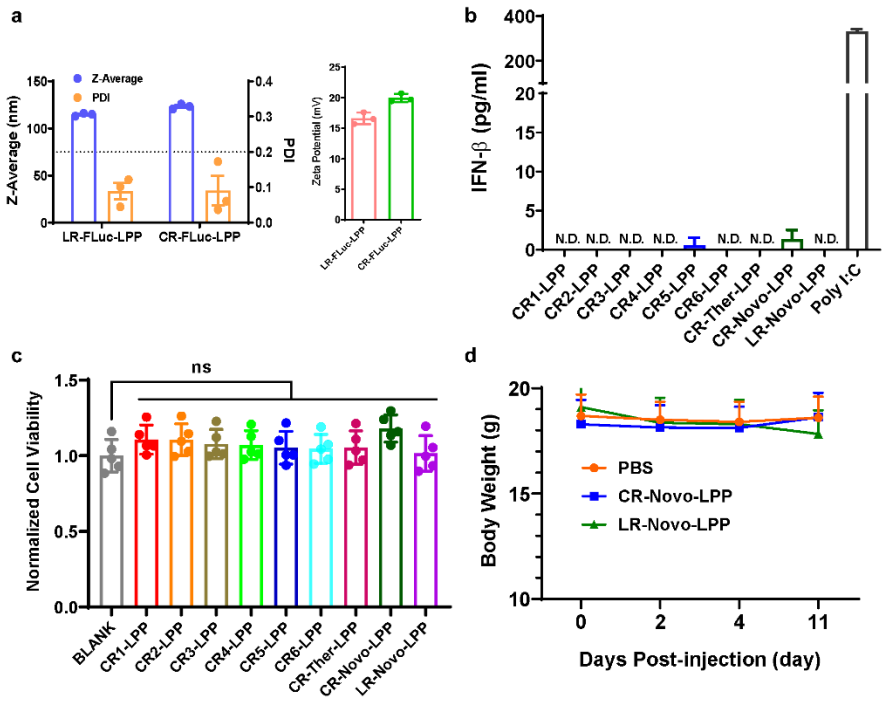

Extended Data Figure 9

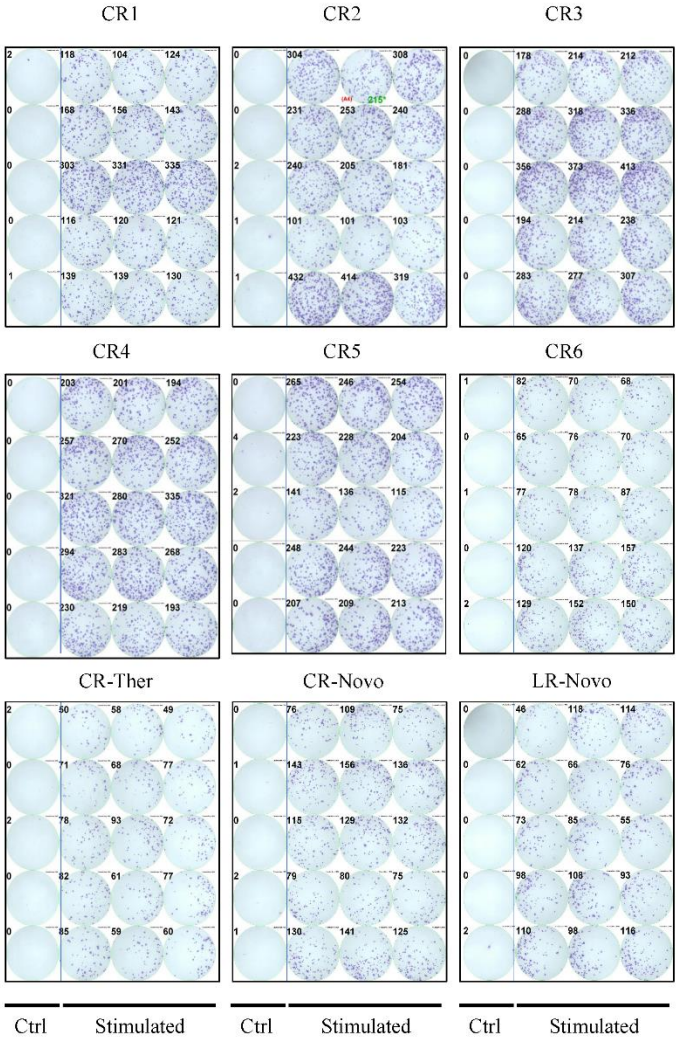

Extended Data Figure 10

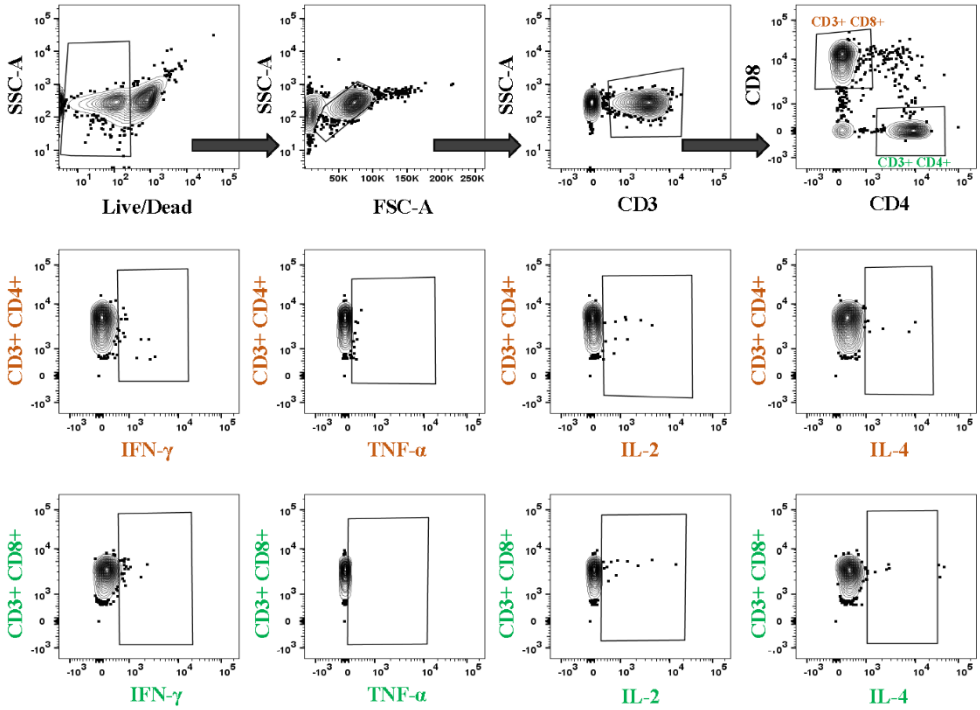

Extended Data Figure 11

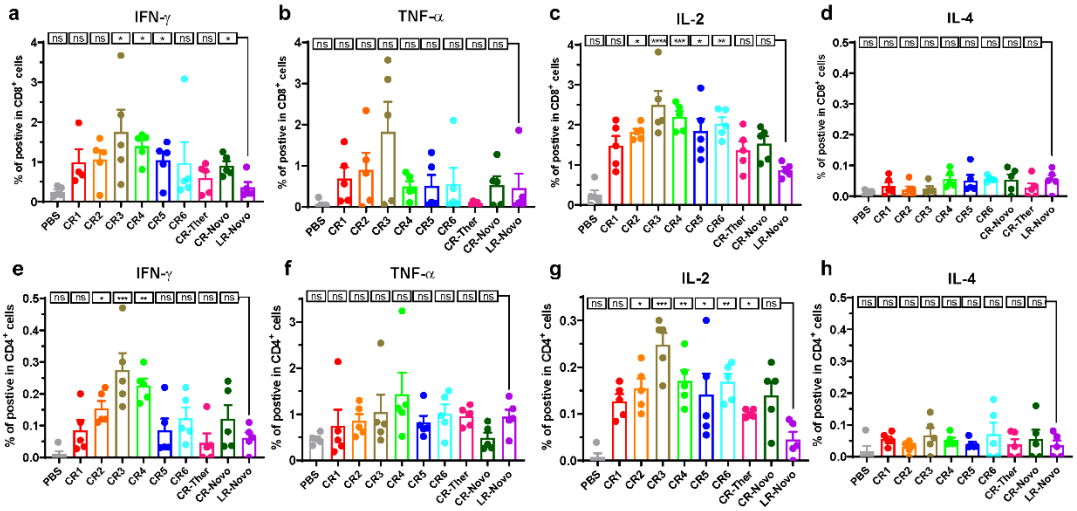

Extended Data Figure 12

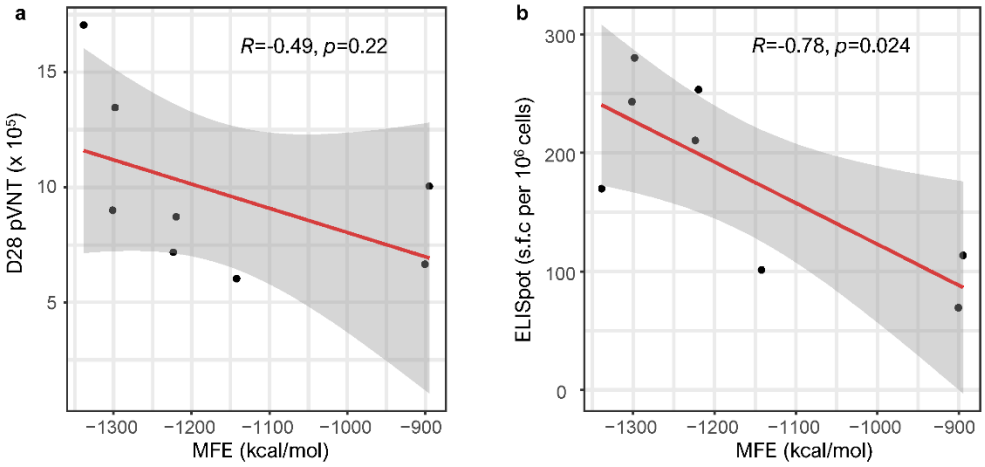

Extended Data Figure 13

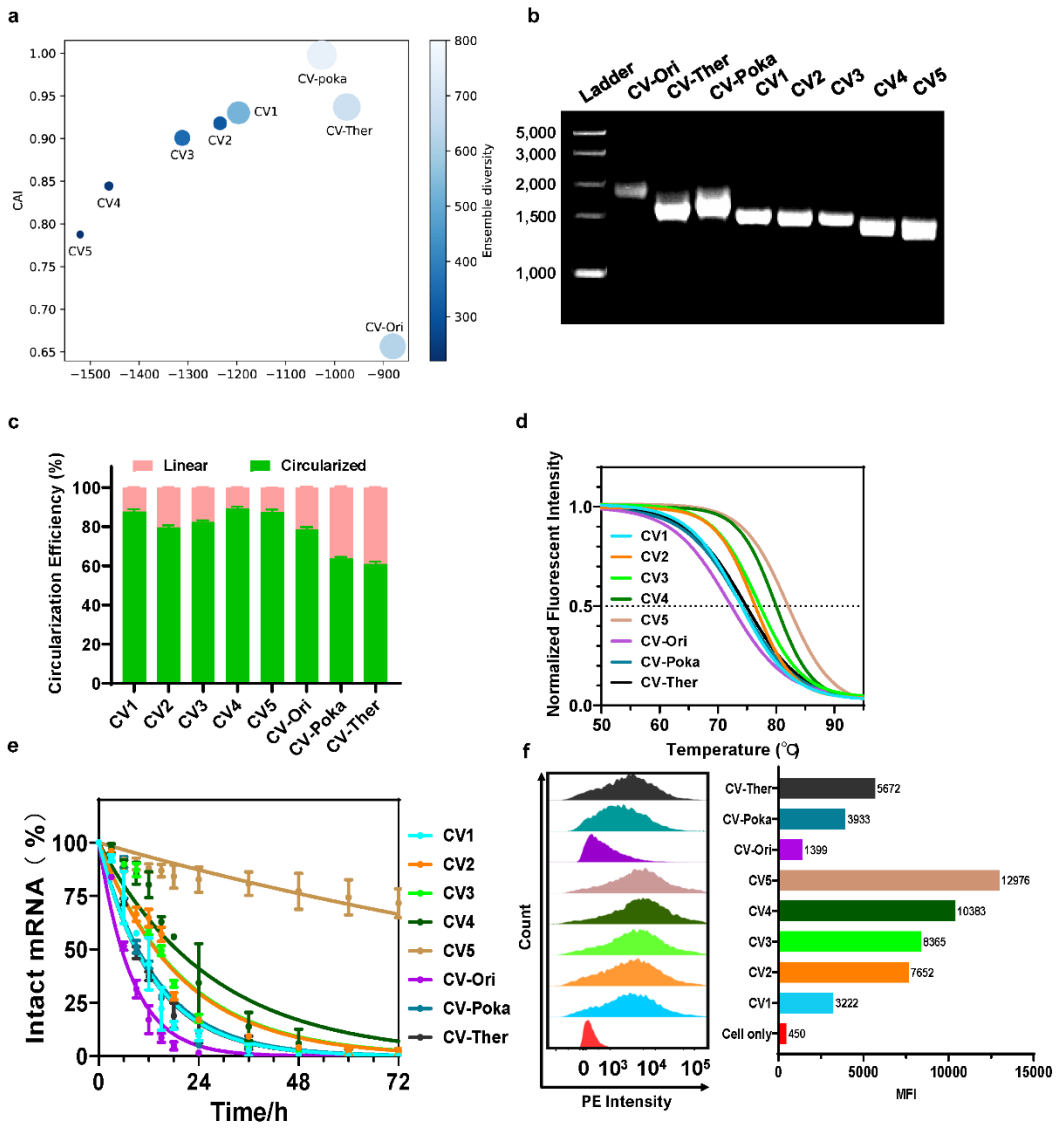

Extended Data Figure 14

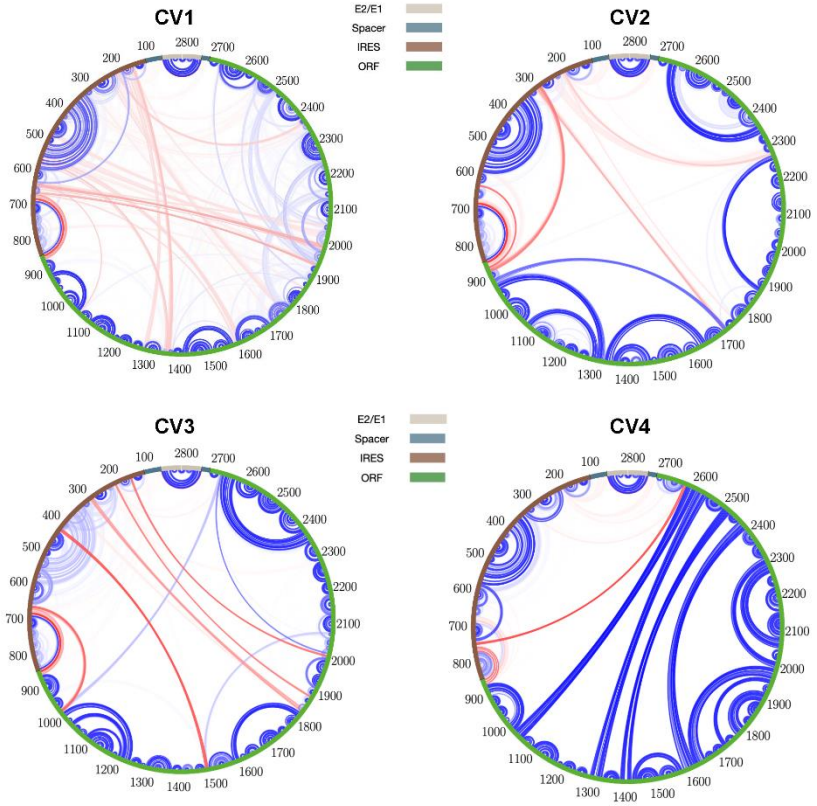

Extended Data Figure 15

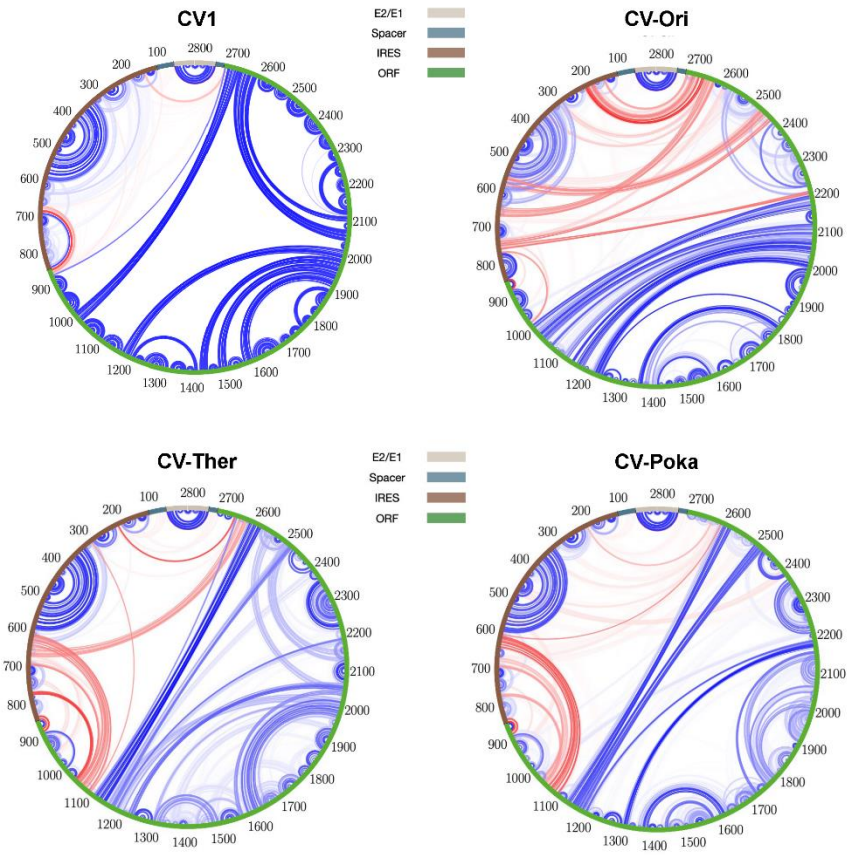

Extended Data Figure 16

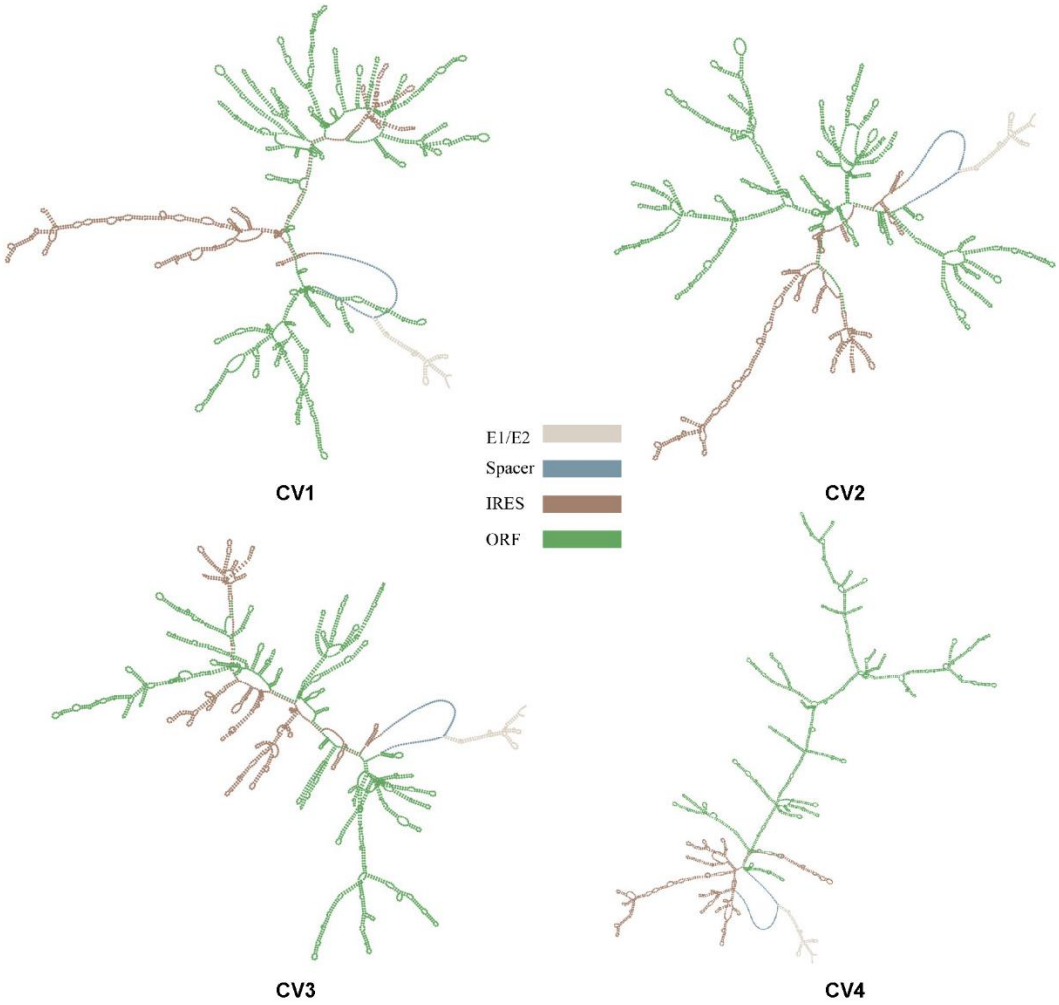

Extended Data Figure 17

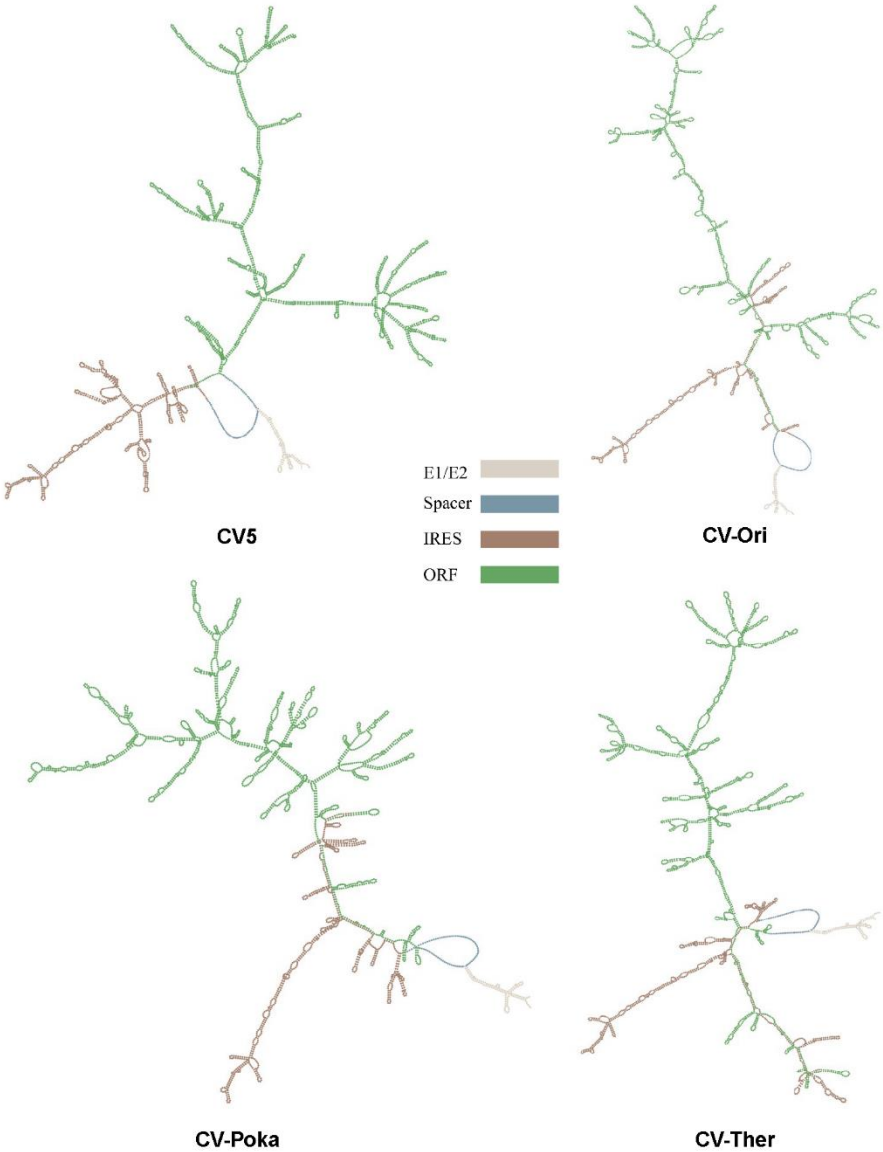

Extended Data Figure 18

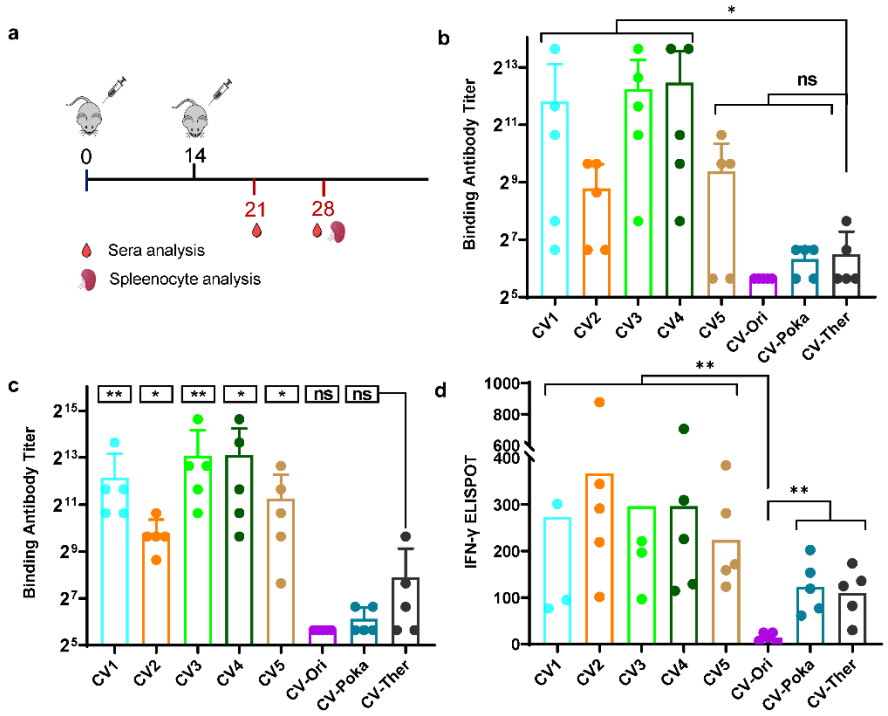

Extended Data Figure 19

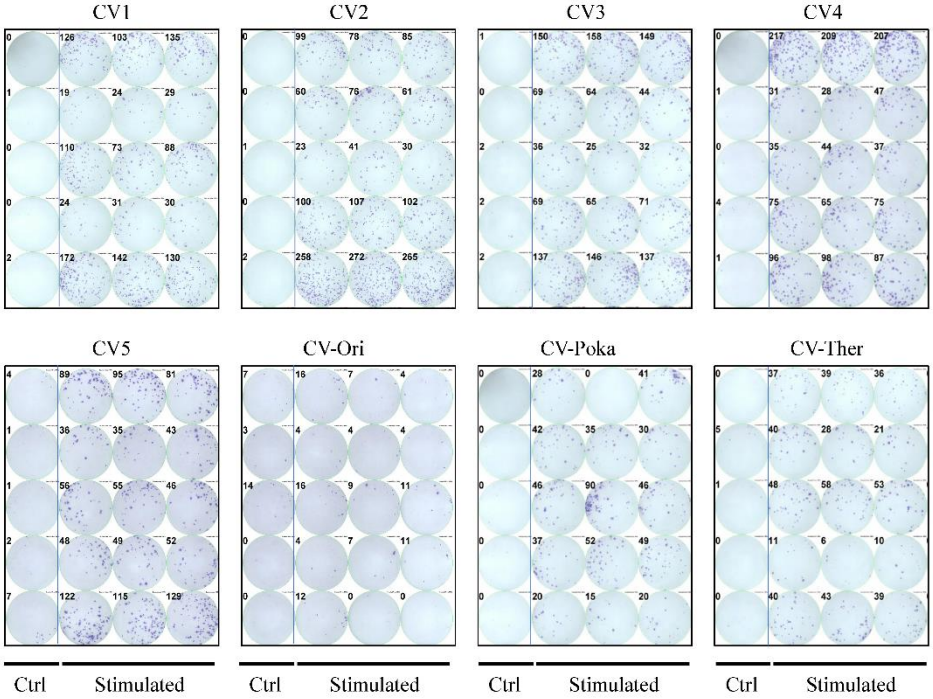

Extended Data Table 1

Seq	MFE (kcal/mol)	CAI	Ensemble Diversity	Positional Entropy	T_m (°C)	Circularization efficiency (%)	In-solution $t_{1/2}$ (h)	Decay constant (10^{-2})	In-cell $t_{1/2}$ (h)	MFI	D28 pVNT	ELISPOT
CR1	-1338.5	0.81	169.11	354.8	79.41	81.53	20.62	3.36	24.34	21979	170511	169.8
CR2	-1301.3	0.81	217.9	483.0	78.08	77.00	16.84	4.12	19.31	22302.7	90007.6	243.1
CR3	-1298.2	0.87	161.46	335.3	78.11	77.93	15.56	4.46	24.55	22826	134644	280.1
CR4	-1219.7	0.87	164.12	337.6	73.92	80.80	12.44	5.57	15.46	22126	87136.5	253.3
CR5	-1223.6	0.93	179.96	377.0	76.18	70.97	12.05	5.75	9.18	22183	71741.8	210.4
CR6	-1142.3	0.93	213.26	447.4	73.38	68.40	11.37	6.10	18.32	17863.7	60288.4	101.2
CR-Ther	-900.6	0.93	609.31	1410.8	68.59	60.80	9.68	7.16	13.60	18295.7	66552.3	69.3
CR-Novo	-894.9	0.82	576.49	1259.2	69.00	61.53	9.14	7.58	10.21	21365	100432	113.4

Extended Data Table 2

Tissue	6h		24h		48h		72h		168h	
	CR-Novo	CR3	CR-Novo	CR3	CR-Novo	CR3	CR-Novo	CR3	CR-Novo	CR3
Injection site	2.21×10^{10}	4.42×10^{10}	1.55×10^{8}	3.11×10^{9}	2.39×10^{7}	9.67×10^{7}	1.06×10^{7}	1.13×10^{8}	5.71×10^{6}	1.89×10^{6}
Lymph node	1.78×10^{7}	1.17×10^{8}	5.52×10^{6}	3.38×10^{8}	3.56×10^{7}	2.71×10^{7}	7.08×10^{7}	2.54×10^{8}	4.10×10^{7}	5.47×10^{7}
Spleen	1.58×10^{8}	1.24×10^{8}	4.17×10^{7}	1.63×10^{8}	3.27×10^{7}	1.11×10^{7}	3.30×10^{7}	1.06×10^{7}	1.22×10^{7}	1.28×10^{7}
Liver	1.90×10^{7}	2.72×10^{7}	2.80×10^{5}	7.35×10^{5}	3.26×10^{5}	9.18×10^{4}	1.98×10^{5}	6.37×10^{4}	1.22×10^{5}	9.60×10^{4}
Lung	7.72×10^{6}	7.84×10^{6}	5.42×10^{5}	1.43×10^{6}	6.71×10^{5}	8.89×10^{5}	1.11×10^{6}	5.96×10^{5}	1.83×10^{5}	1.47×10^{5}
Heart	2.08×10^{7}	5.97×10^{6}	9.14×10^{5}	2.59×10^{5}	3.04×10^{5}	8.53×10^{5}	1.08×10^{5}	4.19×10^{5}	2.03×10^{5}	2.56×10^{5}
Kidney	3.13×10^{6}	2.33×10^{6}	6.71×10^{4}	1.48×10^{5}	1.66×10^{5}	1.01×10^{6}	1.62×10^{5}	3.13×10^{6}	2.04×10^{5}	1.32×10^{5}
Brain	8.59×10^{5}	8.87×10^{5}	2.74×10^{6}	1.73×10^{6}	1.74×10^{5}	3.47×10^{5}	4.17×10^{5}	4.63×10^{5}	1.36×10^{5}	2.37×10^{5}
Sm. Int.	3.85×10^{5}	1.55×10^{6}	1.25×10^{6}	2.26×10^{5}	1.84×10^{5}	1.42×10^{5}	1.55×10^{5}	2.39×10^{5}	1.10×10^{5}	1.35×10^{5}

Extended Data Table 3

Seq	MFE (kcal/mol)	CAI	Ensemble Diversity	Positional Entropy	T_m (°C)	Circularization efficiency (%)	In-solution $t_{1/2}$ (h)	MFI (24h)	D28 Ab GMT	ELISPOT
CV1	-862.80	0.93	525.21	1201.5	73.73	87.6	9.00	24515	4480	272.7
CV2	-899.90	0.92	308.43	647.5	76.20	79.6	13.62	26735	880	366.2
CV3	-979.50	0.90	351.68	728.0	76.85	82.4	13.82	28858	8640	295.8
CV4	-1129.20	0.85	243.61	499.9	79.85	89.3	18.71	27836	8800	296.2
CV5	-1193.80	0.79	228.75	495.3	81.98	87.4	122.2	34402	2440	223.6
CV-Ori	-535.50	0.67	624.23	1431.6	71.92	78.6	5.49	6462	50	13.3
CV-Poka	-679.90	1.00	755.43	1735.4	73.93	63.6	9.39	12204	70	122.4
CV-Ther	-634.00	0.94	676.78	1497.6	74.65	60.9	8.88	19042	240	109.1